

Constraining photon trajectories in black hole shadows

D. Pugliese&Z. Stuchlík*

*Research Centre for Theoretical Physics and Astrophysics,
Institute of Physics, Silesian University in Opava,
Bezručovo náměstí 13, CZ-74601 Opava, Czech Republic*

(Dated: May 24, 2024)

We examine the shadow cast by a Kerr black hole, focusing on constraints on photons corresponding to different shadow boundaries. The photons are related to different orbital ranges and impact parameter values, creating a map of the shadow boundaries. Our analysis fixes also the conditions under which it is possible to observe an “imprint” of the black hole (outer) ergosurface and (outer) ergoregion on the Kerr black hole shadow boundary. The counter-rotating case resulted strongly constrained with respect to the co-rotating case, constituting a remarkable and significant difference where the counter-rotating component associated with the shadow boundary is strongly distinct from the co-rotating one. However, in this framework, even the co-rotating photons imply restrictions on conditions on the spins and planes, which are bounded by limiting values. We believe the results found here, being a tracer for the central black hole, can constitute new templates for the ongoing observations.

Keywords: black hole physics –black hole physics–shadow– accretion discs

I. INTRODUCTION

The first image of the black hole (**BH**) shadow was released by the Event Horizon Telescope (**EHT**) Collaboration¹ in 2019, first results concerning the detection of an event horizon of a super-massive black hole (**SMBH**) at the center of a neighboring elliptical Messier **87** (**M87**) galaxy were announced in [1–6]. The corresponding linear-polarimetric **EHT** images of the center of **M87** were presented in [7]. In [8] the resolved polarization structures (and Atacama Large Millimeter/submillimeter Array observation (**ALMA**)) have been compared to theoretical models. (A new sharper image of the **M87 BH** has been released, in 2023 created with PRIMO algorithm [9]). In 2022 the **EHT** Collaboration has been able to observe the shadow cast by the **SMBH** Sagittarius **A*** (**SgrA***) in the center of our galaxy² [10–15]. The **EHT** observations, providing immediate evidences of an event horizon presence, constitute a consistent advance in astronomy having made also possible to focus on physical phenomena in the close proximity of the **BH**. (The **BH** shadow could be related to complex astrophysical phenomena, typically accretion disks and related jets orbiting close to the horizon³.)

We expect that it will be possible to observe even more refined and clearer details from the astronomical observations in near future (see [28]). There is a continuous improvement (and updating) of the **SMBH M87*** image, through new analyses and simulations. Advancements and new data analysis techniques can allow a more clear observation and description of the **BH** environment and more refined analyses will be able to clearly discern the presence and

* daniela.pugliese@physics.slu.cz

¹ The Event Horizon Telescope: (<https://eventhorizontelescope.org>): a virtual Earth-sized large telescope array consisting of a global network of radio telescopes using very-long-baseline interferometry (**VLBI**) at millimeter and sub-millimeter wavelengths—see also [2], for further information on the instrument.

² The **EHT** images showed rings of synchrotron emissions. The rings appeared asymmetric, consistently with synchrotron emission from a hot plasma orbiting a (Kerr) **BH** (and subjected to gravitational lensing). In particular, the ring morphological characteristics reflect the **BH** parameters (mass and spin). In these models, magnetized **ADAF** (advection-dominated accretion flow) appears to emerge as the underlying best model explaining the observed synchrotron emission. Models of magnetized, radiatively inefficient accretion flow/**ADAFs** have been constructed for **SgrA*** fitting the observed spectral energy density (characteristic low luminosity of **SgrA***, relative to the Eddington limit, appears to suggest matter falling onto the **BH** as radiatively inefficient/**ADAF**). Analytical modelization aims therefore at the description of the emitted synchrotron radiation sources (which could also consist in a magnetized torus, for example, a geometrically thick accretion flow emitting thermal synchrotron) and a jet with thermal and non-thermal synchrotron radiation. Semi-analytic models of synchrotron emission from relativistic jet, general relativistic magnetohydrodynamical (**GRMHD**) simulations of **ADAFs**, distinguish in general two different modes: the standard and normal evolution model (**SANE**), (magnetic fields are turbulent and midplane magnetic field pressure is less than the gas pressure), and the magnetically arrested disk (**MAD**) (strong magnetic fields)—[10–15].

³ The **EHT** reported also observations of Blazar 3C 279 (4C–05.55, NRAO413, PKS1253–05), high resolution images of the jet produced by the **SMBH** sitting at the center of Centaurus A and the distant Blazar J1924-2914 (the radio-loud quasar is also known as (PKS 1921–293, OV–236))—see also [16–20], and the observations of the flat-spectrum radio quasar NRAO 530 (1730-130, J1733–1304)[21].

structure of different photon orbits, as predicted by the theory. In [46], for example, the **M87*** images from **EHT** collaboration has been re-analyzed, using a series of kinetic plasma simulations, predicting the images during the outbursts characterizing **M87***. It was found that, following magnetic-field instabilities, radio-wave hot spots (connected to closed magnetic structures—plasmoids—of the **BH** magnetosphere) may appear as rotating around the **BH** shadow on an orbit three times larger than the **BH** size. In [37], revisiting the past observations, it has been claimed to have spotted the sharp light ring around **M87***—see also [9, 19, 38, 60, 70, 85]. (The ring was predicted by general relativistic magnetohydrodynamical (**GRMHD**) simulations in the near horizon region of **M87***). This new analysis also provides evidence of a rotating jet ejected from the **BH** region [70] and [9, 37, 38, 70, 85, 103, 106, 113]. A recent analysis of **EHT** data sharpened the view of the glowing gas around the **BH**. The new image was reconstructed using the **PRIMO** algorithm, [9]; new observations, obtained combined data from radio telescopes **Global Millimetre VLBI Array**, **ALMA**, and the **Greenland Telescope**, have shown the ring-like accretion structure in **M87** connecting the **BH** plasma jet to the **BH** and the accretion matter[28].

BHs shadows have been studied analytically in numerous studies [32, 42, 73, 102]. The standard notion of the **BH** shadow defines rather the silhouette (shadow boundary) than shadow due to definition of the dark region in radiating screen in situation where the **BH** is located before the screen and the distant observer [32, 34]. The boundary of the shadow is constituted by unstable photon (spherical and circular) orbits [22, 23, 32, 34, 53, 57, 96, 97, 100], whereas the shadow itself is the dark region bounded by shadow boundary. From methodological view—point, in general the **BH** shadow boundary is found considering photons coming from all the points at infinity. The observer is located at infinity, and the **BH** has a well defined and fixed inclination angle⁴. Photons on unstable orbits can reach the far away observer after perturbation. The photons moving towards the **BH** could be trapped in unstable spherical orbits, or they can be captured by **BH** gravitational field producing the central dark region (shadow), or they could escape to infinity, being detected by the distant observer if in line of sight. However, the observed shadow boundary can be substantially modified by properties of the orbiting matter and even by properties of photons radiated by the orbiting matter, depending on properties of the region of the light distribution and its source. Possible source of the light can be the accretion disk orbiting the central **BH**. In these conditions, the photons could interact with the accreting plasma affecting therefore the photons distribution and the intensity. The shadow in this case has been also extensively studied for example in [35, 39, 40, 48, 50, 58, 104].

The shape and size of a **BH** shadow boundary depend in particular on the **BH** parameters. Hence observations of the shadow boundary not only provide compelling **BH** evidence, but also an estimation on the **BH** parameters. In order to fit astronomical observations, several observables were constructed using special points on the shadow boundary in the celestial coordinates (see [103]). These new observables should carry information on the central spinning **BH** and different orbiting structures. In this work we study some aspects of the **BH** shadows boundary analyzing photon spherical orbits in orbital ranges associated to accretion process. In our analysis we solve the equations for the null geodesics constituting the shadow boundary, fixing constraints on the photons impact parameter ℓ or the radius $r = \text{constant}$. In this way we individuate points on the **BHs** shadow profiles correspondent to the fixed constraints on ℓ or r , investigated for all values of the **BH** spin parameter. We consider photons co-rotating and counter-rotating motion (determined by ℓ). We also explore the effects of frame dragging on the shadow boundary, investigating the possibility to observe an “imprint” of the outer ergoregion and the outer ergosurface on the shadows boundary, by examining the photon spherical orbits in the outer ergoregion and on the outer ergosurface.

The structure of this article is as follows. In Sec. (II) we introduce the spacetime metric. Constants of motion and geodesics equations are summarized in Sec. (II A). Black hole shadows are introduced in Sec. (III). Shadows analysis is in Sec. (IV). We investigate shadows for specific impact parameter in Sec. (IV A), while in Sec. (IV B) solutions are analysed for fixed r related to particular spherical orbital ranges. In Sec. (IV C) photons spherically orbiting on the outer ergosurface, and in the outer ergoregion are investigated. Concluding remarks are in Sec. (V). In Appendix (A) there are further notes on the Kerr spacetime geodesic structure. In Appendix (B) various aspects of the analysis have been further detailed.

⁴ The angle between the **BH** rotation axis and the observer line of sight.

II. THE SPACETIME METRIC

In the Boyer-Lindquist (BL) coordinates $\{t, r, \theta, \phi\}$ ⁵, the Kerr spacetime line element reads

$$ds^2 = - \left(1 - \frac{2Mr}{\Sigma}\right) dt^2 + \frac{\Sigma}{\Delta} dr^2 + \Sigma d\theta^2 + \left[(r^2 + a^2) + \frac{2Mra^2}{\Sigma} \sin^2 \theta\right] \sin^2 \theta d\phi^2 - \frac{4rMa}{\Sigma} \sin^2 \theta dt d\phi, \quad (1)$$

$$\text{where } \Delta \equiv a^2 + r^2 - 2rM \quad \text{and} \quad \Sigma \equiv a^2(1 - \sin^2 \theta) + r^2. \quad (2)$$

Parameter $a = J/M \geq 0$ is the metric spin, where total angular momentum is J and the gravitational mass parameter is M . A Kerr **BH** is defined by the condition $a \in [0, M]$. The extreme Kerr **BH** has dimensionless spin $a/M = 1$. The non-rotating case $a = 0$ is the Schwarzschild **BH** solution. (The Kerr naked singularities (**NSs**) have $a > M$.)

The **BH** horizons are

$$r_- \leq r_+, \quad \text{where} \quad r_{\pm} \equiv M \pm \sqrt{M^2 - a^2}. \quad (3)$$

The outer ergoregion of the spacetime is $]r_+, r_{\epsilon}^+]$, where the outer ergosurface r_{ϵ}^+ is

$$r_{\epsilon}^+ \equiv M + \sqrt{M^2 - a^2(1 - \sigma)} \quad \text{with} \quad \sigma \equiv \sin^2 \theta \in [0, 1], \quad (4)$$

and there is $r_{\epsilon}^+ = 2M$ in the equatorial plane ($\sigma = 1$), and $r_+ < r_{\epsilon}^+$ on $\theta \neq 0$.

In the following, we will use dimensionless units with $M = 1$ (where $r \rightarrow r/M$ and $a \rightarrow a/M$).

A. Geodesics equations and constants of motion

The equatorial plane is the symmetry plane for the metric, and the constant r orbits on this plane are circular. The geodesic equations in Kerr spacetime are fully separable. There are four constants of motion. For convenience we summarize the (Carter) equations of motion as follows (see [41]):

$$\dot{t} = \frac{1}{\Sigma} \left[\frac{P(a^2 + r^2)}{\Delta} - a[a\mathcal{E}\sigma - \mathcal{L}] \right], \quad \dot{r} = \pm \frac{\sqrt{R}}{\Sigma}; \quad \dot{\theta} = \pm \frac{\sqrt{T}}{\Sigma}, \quad \dot{\phi} = \frac{1}{\Sigma} \left[\frac{aP}{\Delta} - \left[a\mathcal{E} - \frac{\mathcal{L}}{\sigma} \right] \right]; \quad (5)$$

for $p^{\alpha} = dx^{\alpha}/d\tau \equiv u^{\alpha} \equiv \{\dot{t}, \dot{r}, \dot{\theta}, \dot{\phi}\}$, the geodesic tangent four-vector, where τ is an affine parameter, normalized so that $p^{\alpha}p_{\alpha} = -\mu^2$, and μ is the rest mass of the test particle where a null geodesics has $\mu = 0$ ⁶, and

$$P \equiv \mathcal{E}(a^2 + r^2) - a\mathcal{L}, \quad R \equiv P^2 - \Delta[(\mathcal{L} - a\mathcal{E})^2 + \mu^2 r^2 + \mathcal{Q}], \quad T \equiv \mathcal{Q} - (\cos \theta)^2 \left[a^2(\mu^2 - \mathcal{E}^2) + \left(\frac{\mathcal{L}^2}{\sigma} \right) \right], \quad (6)$$

where \mathcal{Q} is the Carter constant of motion. Quantities $(\mathcal{E}, \mathcal{L})$ are constants of geodesic motions

$$\mathcal{E} = -(g_{t\phi}\dot{\phi} + g_{tt}\dot{t}), \quad \mathcal{L} = g_{\phi\phi}\dot{\phi} + g_{t\phi}\dot{t}, \mu^2, \quad (7)$$

defined from the Kerr geometry rotational Killing field $\xi_{\phi} \equiv \partial_{\phi}$, and the Killing field $\xi_t \equiv \partial_t$ representing the stationarity of the background.

The constant \mathcal{L} in Eq. (7) may be interpreted as the axial component of the angular momentum of a test particle following timelike geodesics. Constant \mathcal{E} represents the energy of the test particle related to the static observers at infinity⁷. We introduce also the specific angular momentum (called also impact parameter)

$$\ell \equiv \frac{\mathcal{L}}{\mathcal{E}} = -\frac{g_{\phi\phi}u^{\phi} + g_{t\phi}u^t}{g_{tt}u^t + g_{\phi t}u^{\phi}}, \quad (8)$$

With $a > 0$, the fluids and particles counter-rotation (co-rotation) is defined by $\ell a < 0$ ($\ell a > 0$).

Static observers, having four-velocity $\dot{\theta} = \dot{r} = \dot{\phi} = 0$, cannot exist inside the ergoregion. Whereas, trajectories $\dot{r} \geq 0$, including photons crossing the outer ergosurface and escaping outside in the region $r \geq r_{\epsilon}^+$ are possible.

⁵ We adopt the geometrical units $c = 1 = G$ and the $(-, +, +, +)$ signature, Latin indices run in $\{0, 1, 2, 3\}$. The radius r has unit of mass $[M]$, and the angular momentum units of $[M]^2$, the velocities $[u^t] = [u^r] = 1$ and $[u^{\theta}] = [u^{\phi}] = [M]^{-1}$ with $[u^{\phi}/u^t] = [M]^{-1}$, $[u_{\phi}/u_t] = [M]$ and an angular momentum per unit of mass $[\mathcal{L}]/[M] = [M]$.

⁶ For the seek of simplicity we adopted notation \dot{q} or u^{α} for photons and particles, the context should avoid any possible misunderstanding.

⁷ Note, we assume $\mathcal{E} > 0$ (and $\dot{t} > 0$). This condition for co-rotating fluids in the ergoregion has to be discussed further. In the ergoregion particles can also have $\mathcal{L} = 0$ (i.e. $\ell = 0$). However this condition characterizing the ergoregion is not associated to geodesic circular motion in the **BH** spacetimes. There are no solutions in general for $\dot{t} \geq 0$, $\mathcal{E} < 0$ $T \geq 0$ and $\ell < 0$ (for $r > r_+$, $a \in [0, 1]$, $\sigma \in [0, 1]$). We assume the so-called positive root states $\dot{t} > 0$ —for details see [31, 36, 77]

III. SHADOWS

In this section we discuss the concept of **BH** shadows, introducing the quantities (q, ℓ) (constants of motion), the celestial coordinates (α, β) and we discuss the constraints adopted in our analysis.

Focusing on the null geodesic equations (5), the boundary of the **BH** shadow is determined by the (unstable) photon orbits defined by:

$$R = \partial_r R = 0, \quad \partial_r^2 R > 0, \quad (9)$$

hereafter referred as set (\mathfrak{R}) of equations, within constraints provided by the set⁸ of Eqs (5).

We introduce the motion constants q and ℓ (impact parameter)

$$\ell \equiv \frac{\mathcal{L}}{\mathcal{E}}, \quad q \equiv \frac{\mathcal{Q}}{\mathcal{E}^2}. \quad (10)$$

Following [32] we assume the observer is located at infinity (i.e. at very large distance in practical calculation), introducing the celestial coordinates⁹ α and β for the null geodesics

$$\alpha = -\frac{\ell}{\sqrt{\sigma}}, \quad \beta = \pm\sqrt{q - q_c} \quad (11)$$

$$\text{for } \sigma \neq 0 \text{ and } q \geq q_c, \quad \text{where } q_c \equiv \frac{(1 - \sigma)(\ell^2 - \ell_c^2)}{\sigma}, \quad \ell_c^2 \equiv a^2\sigma.$$

The shadow boundary is, at fixed spin a and angle σ , a closed curve in the plane $\alpha - \beta$, and its points correspond to constant r , (solutions of (\mathfrak{R})), q and parameter¹⁰ ℓ .

In this work we study the solutions (r, q, ℓ) , corresponding to the points (α, β) of the shadow boundary, then analysing the variation of (r, q, ℓ) with (a, σ) . In order to do this, r and ℓ are set in ranges defined by some boundary values. We then proceed by solving system (\mathfrak{R}) for the boundary r and ℓ values, obtaining, for fixed radius r , the solutions (α, β, ℓ, q) and, for fixed parameter ℓ , solutions (α, β, r, q) , then analyzed for all values of a and σ . Ultimately, we obtain the parts of the shadow boundary associated to the fixed constraints, and therefore a shadow boundary map (in dependence on the selected ranges of values for ℓ or r for all possible values of (a, σ)). Below we discuss the limit values for r and ℓ .

In Sec. (IV C) we solve system (\mathfrak{R}) for fixed $r \in]r_+, r_\epsilon^+]$. Solutions are unstable spherical photon orbits located in the outer ergoregion and on the outer ergosurface. The frame-dragging effects on the **BH** shadow profile are explored also studying the solutions of the equations (\mathfrak{R}) for $\dot{\phi} = 0$, i.e. for null geodesics, with $\ell < 0$, on an inversion surface[94]. An inversion surface is a closed surface, defined by condition $\dot{\phi} = 0$ on the geodesics, embedding a Kerr **BH**, and located out of the Kerr **BH** outer ergosurface, which can be seen as effect of the Kerr spacetime frame-dragging-Figs (1). We use the notation $Q_\mathbf{T}$ for any quantity Q considered at the inversion point, where within the condition $\dot{\phi} = 0$, there is $\ell = \ell_\mathbf{T} \equiv -\frac{gt_\phi}{g_{tt}} \Big|_\mathbf{T}$.

For the other limiting values, we will consider radii $\{r_\gamma^\pm, r_{mbo}^\pm, r_{mso}^\pm\}$ and, for the parameter ℓ , the functions $\{\ell_{mso}^\pm, \ell_{mbo}^\pm, \ell_\gamma^\pm\}$, defined in Appendix (A) for co-rotating $(-)$ and counter-rotating $(+)$ motion. (There is Q_\bullet for any quantity Q evaluated at r_\bullet .) Radii $r_\gamma^\pm(a)$ are photon circular orbits on the equatorial plane¹¹. They are solutions of (\mathfrak{R}) for $\sigma = 1$ ($q = 0$) and $\ell = \ell_\gamma^\pm(a)$ respectively. Radii r_{mbo}^\pm are the marginal circular bound orbits, and radii r_{mso}^\pm are marginal stable circular orbits for time-like particles on the equatorial plane, having $\ell = \ell_{mbo}^\pm$ and $\ell = \ell_{mso}^\pm$ respectively [34]. Therefore, radii $\{r_{mbo}^\pm, r_{mso}^\pm\}$ cannot be solutions of (\mathfrak{R}) with $\ell^\pm \in \{\ell_{mso}^\pm, \ell_{mbo}^\pm\}$ respectively, $q = 0$ and $\sigma = 1$. However, here we solve (\mathfrak{R}) on the *spherical surfaces* defined by radii $\{r_{mbo}^\pm, r_{mso}^\pm, r_\gamma^\pm\}$, examining the unstable photons circular orbits (solutions of (\mathfrak{R})) on $r = \{r_{mbo}^\pm, r_{mso}^\pm, r_\gamma^\pm\}$ for a *general* angle σ and constants¹² (ℓ, q) .

⁸ In this work we also consider solution $\partial_r^2 R = 0$. Note R does not depend explicitly on σ . (In particular we shall consider also the condition $T \geq 0$). There are no solutions for $t \geq 0$, $\mathcal{E} < 0$, $T \geq 0$, $\ell > 0$, $R = 0$, $R' = 0$.

⁹ Note we can define $\alpha = -\ell/\sin\theta$ where $\alpha = -\ell$ and $\beta = \pm\sqrt{q}$ (where $q \geq 0$) for $\theta = \pi/2$. Definition $\alpha = -\ell/\sqrt{\sigma}$ is equivalent to consider $\theta \in [0, \pi]$.

¹⁰ For example, conditions $(R = 0, R' = 0)$ for $a = 0$ and $q = 0$ correspond to $(r = 3, \ell = \pm 3\sqrt{3})$, photon orbit on the equatorial plane of the Schwarzschild spacetime (where there is $R'' > 0$), and point $(\alpha, \beta) = (\mp 3\sqrt{3}, 0)$ of the Schwarzschild **BH** shadow boundary.

¹¹ For the definition in relation to the photon sphere see for example [43, 60, 86, 105, 114].

¹² That is, considering for example the radius r_{mbo}^\pm , defining a spherical surface embedding the **BH**, a solution of (\mathfrak{R}) can exist on this surface on an angle $\sigma \neq 1$, a constant $q \neq 0$ and $\ell \neq \ell_{mbo}^\pm$. The corresponding solutions (σ, q, ℓ) are then detailed studied in Sec. (IV B), with the corresponded point (α, β) on the shadow boundary and studied at the variation of a .

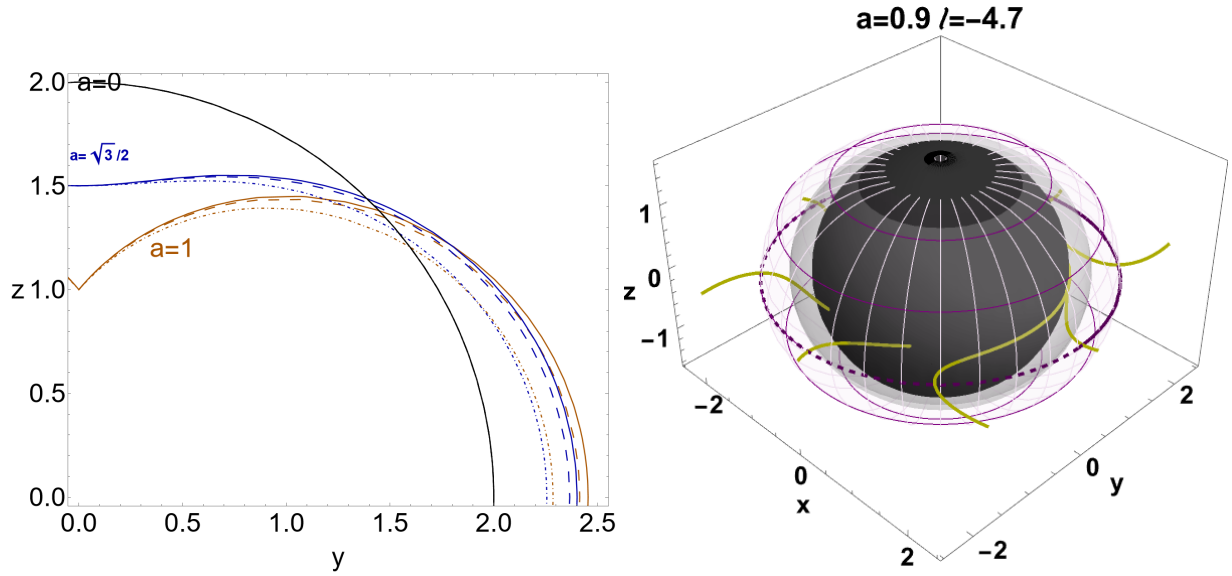


FIG. 1. Left panel: inversion surfaces sections, for ℓ_{mso}^+ (plain) and ℓ_{mbo}^+ (dashed), ℓ_γ^+ (dotted-dashed). It is $r = \sqrt{y^2 + z^2}$ and $\theta = \arccos(z/r)$. Right panel: counter-rotating photon orbits (yellow curves) to the **BH** (black region). Inversion point $r_{\mathbf{T}}$ is the deep-purple curve. It is $\{z = r \cos \theta, y = r \sin \theta \sin \phi, x = r \sin \theta \cos \phi\}$. Gray region is the outer ergosurface, light-purple region is $r < r_{\mathbf{T}}(\sigma_{\mathbf{T}})$.

Similarly, we find solutions of (\mathfrak{R}) for spherical photon orbits with parameter $\ell^\pm \in \{\ell_{mso}^\pm, \ell_{mbo}^\pm, \ell_\gamma^\pm\}$ at a *general* radius r , a general angle σ and constant¹³ q .

The spherical surfaces $\{r_{mbo}^\pm, r_{mso}^\pm, r_\gamma^\pm\}$ can provide an immediate astrophysical context in relation to the structures orbiting around the **BH**¹⁴. In fact, the accretion disk inner edge (cusp) orbiting on the **BH** equatorial plane is located in region $r \in]r_{mbo}^\pm, r_{mso}^\pm]$ ¹⁵ of the equatorial plane, and therefore, close to $\sigma = 1$, the inner region of an axially symmetric counter-rotating or co-rotating accretion torus is in the spherical shell $]r_{mbo}^\pm, r_{mso}^\pm]$ respectively. The inner orbital shell, $[r_\gamma^\pm, r_{mbo}^\pm]$, covers on the equatorial plane the cusps of the open (hydrodynamical) toroidal structures corresponding to matter funnels along the **BH** rotational axis, which are generally associated to geometrically thick accretion tori,– [25, 62, 67, 74, 75, 92, 95, 99].

In geometrically thin disks, the flows, freely falling from the cusps can be considered leaving the marginally stable circular orbit with $\ell = \ell_{mso}^\pm$, and more in general with $\mp \ell^\pm \in]\mp \ell_{mbo}^\pm, \mp \ell_{mso}^\pm]$ from $]r_{mbo}^\pm, r_{mso}^\pm]$ (or $\mp \ell^\pm \in [\mp \ell_{mbo}^\pm, \mp \ell_\gamma^\pm[$ according to the cusp location in $]r_\gamma^\pm, r_{mbo}^\pm]$ for the open configurations). These momenta also fix the range of location of the accretion disk center, defined as the maximum pressure point in the disks—see Appendix (A).

Hence, in Sec. (IV A) we investigate the solutions of (\mathfrak{R}) , for $\ell \in \{\ell_{mso}^\pm, \ell_{mbo}^\pm, \ell_\gamma^\pm, \ell_{\mathbf{T}}^\pm\}$, in terms of orbit r , constant q , angle σ , and coordinates (α, β) . In Sec. (IV B) we examine the solutions of (\mathfrak{R}) , for $r = \{r_\gamma^\pm, r_{mbo}^\pm, r_{mso}^\pm\}$, and in the spherical shells $r \in [r_{mbo}^\pm, r_{mso}^\pm]$, $r \in [r_\gamma^\pm, r_{mbo}^\pm]$, in terms of parameter ℓ and $(q, \sigma, \alpha, \beta)$.

¹³ In fact, a solution of (\mathfrak{R}) with ℓ_{mbo}^\pm , for example, can exist on an orbit $r \neq r_{mbo}^\pm$, for $\sigma \neq 1$ and a constant $q \neq 0$. The solutions (r, q, σ) are then detailed studied in Sec. (IV A), with the corresponded point (α, β) on the shadow boundary, and studied at the variation of a .

¹⁴ There is $\mp \ell_{mso}^\pm \leq \mp \ell_{mbo}^\pm \leq \mp \ell_\gamma^\pm$ and $r_{mso}^\pm > r_{mbo}^\pm > r_\gamma^\pm$, being valid separately for the upper and lower signs. However, it is important to stress that the relation between the (\pm) limiting impact parameters, and the relative location of the (\pm) orbital spherical shells, defined by the radii $(r_{mso}^\pm, r_{mbo}^\pm, r_\gamma^\pm, r_\epsilon^\pm(a), r_{\mathbf{T}}(a, \ell_{\mathbf{T}}^\pm))$, depend not trivially on the **BH** spin, as it can be easy seen by plotting the functions with respect to the **BH** spin— see Figs (3) and [94].

¹⁵ This assumption is widely adopted (and well grounded) in **BH** Astrophysics, and in the following analysis we will use this assumption independently of other specific details of the accretion disk models.

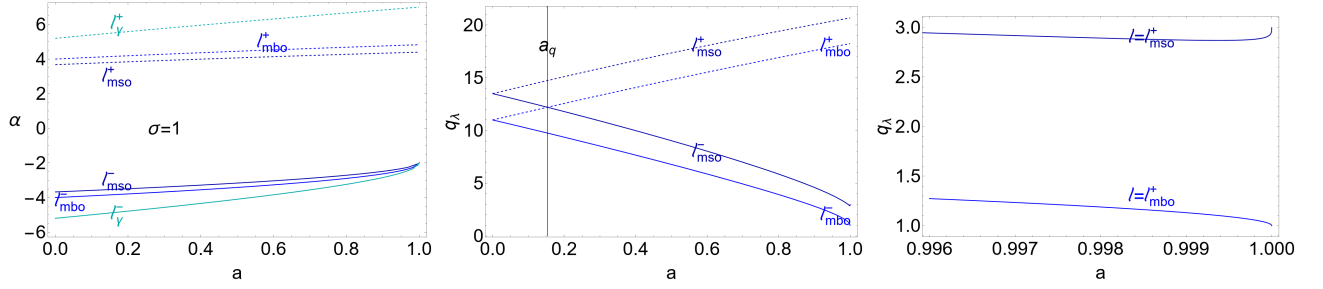


FIG. 2. For $\ell \geq 0$ there is $\alpha \leq 0$ respectively, and solutions $(-\alpha)$ are not represented. Quantity q_λ is in Eq. (12), spin a_q is in Eqs (17). Right panel is a close up view of the center panel.

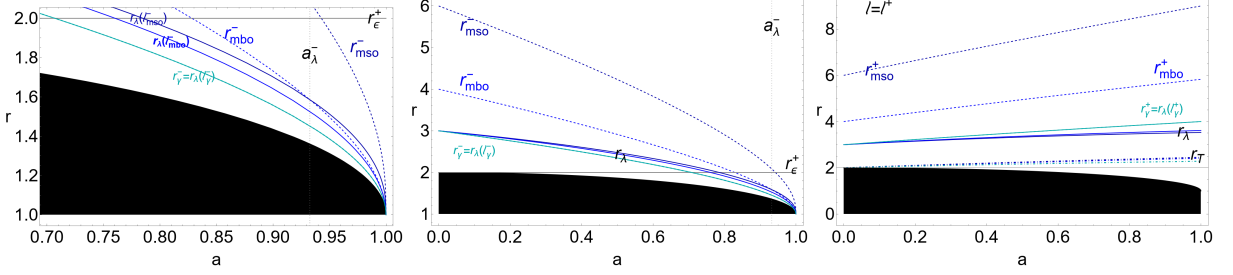


FIG. 3. Radius r_λ (solid curves) and $r_{\mathbf{T}}$ (right panel: dotted-dashed curves) are plotted for $\ell \in \{\ell_\gamma^\pm, \ell_{mbo}^\pm, \ell_{mso}^\pm\}$ (cyan, blue, darker-blue) together with the radii $\{r_\gamma^\pm, r_{mbo}^\pm, r_{mso}^\pm\}$ (dashed curves). Spin a_λ^- is in Eq. (B1). Left panel is a close-up view of the center panel.

IV. SHADOWS ANALYSIS

A. Parameters $\ell \in \{\ell_{mso}^\pm, \ell_{mbo}^\pm, \ell_\gamma^\pm, \ell_{\mathbf{T}}\}$

In general for **BHs** with spin¹⁶ $a \in]0, a_g[$, spherical photon orbits, solutions of system (\mathfrak{A}) with $\ell \in \{\ell_{mso}^\pm, \ell_{mbo}^\pm\}$, are on radius $r = r_\lambda \neq \{r_{mso}^\pm, r_{mbo}^\pm\}$ with motion constant $q = q_\lambda \geq 0$, where

$$a_g(\ell) \equiv \frac{4\ell}{\ell^2 + 4} = -\frac{4\alpha\sqrt{\sigma}}{\alpha^2\sigma + 4} \quad \text{and} \quad q_\lambda \equiv \frac{r[a^2(r+2) - 4a\ell + r^3 - (r-2)\ell^2]}{\Delta}, \quad r_\lambda \equiv \frac{3 - a(a+\ell)}{\sqrt[3]{3}\sqrt[3]{\lambda}} + \frac{\sqrt[3]{\lambda}}{3^{2/3}} \quad (\text{B12})$$

where $\lambda \equiv \frac{1}{6}\sqrt{[54(1-a^2)]^2 + 108[a(a+\ell) - 3]^3 + 9(1-a^2)}$. Functions (q_λ, r_λ) will be further constrained when evaluated for $\ell \in \{\ell_{mso}^\pm, \ell_{mbo}^\pm\}$, as we discuss in details below. In Appendix (B), various aspects of the analysis have been further detailed.

First, by using the condition $T \geq 0$ (and $\dot{t} > 0$), we find that for $a \in]0, 1[$ there is $\sigma \in [\sigma_\lambda, 1]$ and, for the Schwarzschild **BH**, solutions exist for $\sigma \in [\sigma_\ell, 1]$, where σ_ℓ and σ_λ are

$$\sigma_\ell \equiv \frac{\ell^2}{q + \ell^2}, \quad \sigma_\lambda \equiv \frac{q + \ell^2 - a^2 \left[\sqrt{\frac{(q+\ell^2)^2}{a^4} + \frac{2(q-\ell^2)}{a^2}} + 1 - 1 \right]}{2a^2}. \quad (\text{B13})$$

Therefore, σ is bottom bounded by a value σ_ℓ or σ_λ , depending on the **BH** spin and the Carter constant. The limiting angle σ_λ is shown in Figs (4) for $\ell \in \{\ell_{mso}^\pm, \ell_{mbo}^\pm\}$ for **BHs** with spin $a \in [0, 1]$. It is clear how σ_λ changes for the co-rotating and counter-rotating case, and for slowly spinning and fast spinning **BHs** for value $\ell = \ell_{mso}^\pm$. Solutions r_λ , for $\ell \in \{\ell_{mso}^\pm, \ell_{mbo}^\pm, \ell_\gamma^\pm, \ell_{\mathbf{T}}\}$, are shown in Figs (3) together with radii $\{r_{mso}^\pm, r_{mbo}^\pm, r_\gamma^\pm, r_{\mathbf{T}}\}$. Solutions $(\sigma_\lambda, q_\lambda)$,

¹⁶ Spin a_g is expression of the **BH** horizons in terms of the (horizons) specific angular momentum ℓ and, can be expressed in terms of the α celestial coordinate and the angle σ —see Figs (24). The **BH** horizons angular momentum $\ell_H^\pm \equiv 1/\omega_H^\pm$, where $\omega_H^\pm(a) \equiv r_\mp/2a$ are the **BH** horizons frequencies (relativistic angular velocity), are related to parameter ℓ —[88].

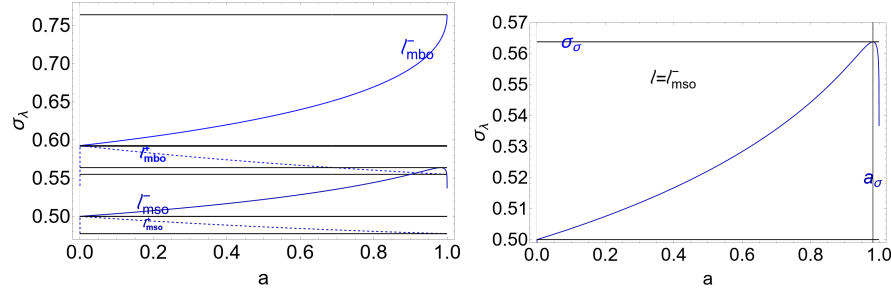


FIG. 4. Quantity σ_λ of Eq. (13) for $\ell \in \{\ell_{mso}^\pm, \ell_{mbo}^\pm\}$. Left panel is a close-up view of the right panel. Maximum value $(a_\sigma, \sigma_\sigma)$ is in Eq. (B1).

relative to the cases $\ell \in \{\ell_{mso}^\pm, \ell_{mbo}^\pm, \ell_\gamma^\pm, \ell_\Gamma\}$, are shown in Figs (2,4). In Fig. (2)–left panel we also show the celestial coordinate α as function of the **BH** dimensionless spin a , for $\sigma = 1$, evaluated on the parameter $\ell \in \{\ell_{mso}^\pm, \ell_{mbo}^\pm, \ell_\gamma^\pm\}$.

Parameter $\ell = \ell_{mso}^-$

The case $\ell = \ell_{mso}^-$ is illustrated in Figs (5), where we show the first results of the analysis for this constraint by giving the constrained β as a function of the spin a for *all* possible σ (left upper panel), and as function of the angle σ for *each* **BH** spin a (central upper panel), and finally as function of the celestial coordinate α for $\sigma \in [0, 1]$ and for different a , as signed on the curves. Each point of a curve is for a different σ . These panels provide immediate information on the parts of shadow boundary correspondent to null geodesics with $\ell = \ell_{mso}^-$ for different (σ, a) . Lower panels summarize the results for this constraint, by relating the coordinates (β, α) to (r, q) , in the entire range of possible a and σ .

Thus, as clear also from Figs (5), photons with $\ell = \ell_{mso}^-$ can be observed for large latitudes, i.e. $\sigma \gtrsim 0.53$. The coordinate β (in magnitude) increases with σ and decreases with a for $\sigma < \sigma_\sigma$ and $a < a_\sigma$ (where $a_\sigma \equiv 0.98217$, and $\sigma_\sigma \equiv 0.563773$ –see Figs (4)).

Considering β for different a and σ , it is clear that difference appears for large latitude angles, i.e. $\sigma > \sigma_\sigma$, and small $\sigma \in [0.53, \sigma_\sigma]$. Angle σ_σ (and spin $a = a_\sigma$) is a critical value where there can be $\beta = 0$. With $\sigma > \sigma_\sigma$ and $a > a_\sigma$, solutions appear for small values of (β, α) in magnitude. The external regions of the plane $\alpha - \beta$, correspondent to the larger values of (β, α) in magnitude, distinguish slower from faster spinning **BHs**, and the smaller ($\sigma \approx 0.56$) from larger latitudinal angles.

From Figs (2,3) we see that r_λ and q_λ are constant for fixed a and different α (and confirmed also by Figs (5)). The radius $r \in [1, 3]$ and parameter q decrease with the **BH** dimensionless spin and the β in magnitude and q ranges decrease with the **BH** spin. The celestial coordinate α is negative, since $\ell > 0$. As shown in Figs (5) and Fig. (2) the magnitude α decreases with a and q , increases with r and the range of α values increases with r and decreases with a .

Parameter $\ell = \ell_{mso}^+$

Photons with $\ell = \ell_{mso}^+$ are considered in Figs (6). It is clear how $|\beta|$ increases with the **BH** spin and the angle $\sigma > 0.479$. For $\sigma > 0.55$ there is $|\beta| > 0$. For this constraint, small values of (α, β) (in magnitude), i.e. the inner regions of the $\alpha - \beta$ plane, characterize slowly spinning **BHs**. From Figs (8)–lower panels (and Fig. (2) it is clear as r and q are constant for different (σ, β, α) . The radius r_λ and the quantity q_λ are larger then in for $\ell = \ell_{mso}^-$, increasing with the **BH** spin. The range of values of the celestial coordinate β increases with (r, a) . On the other hand, the range of values for the α coordinate increases with (r, a, q) .

Parameter $\ell = \ell_{mbo}^+$

Figs (7) present the results for $\ell = \ell_{mbo}^+$. Coordinate $|\beta|$ increases with the angle $\sigma > 0.55$ and the **BH** spin a . For $\sigma \gg 0.58$ there is $|\beta| > 0$. Smaller values of (α, β) (in magnitude), coincident with the inner regions of the $\alpha - \beta$ plane, identify the slowly spinning **BHs**. $|\beta|$ also increases with (a, r, q) , according to Figs (7). Quantities r and q increase with a .

Parameter $\ell = \ell_{mbo}^-$

The case $\ell = \ell_{mbo}^-$ is in Figs (8). Celestial coordinate $|\beta|$ decreases with spin and increases with $\sigma > 0.593$. These curves for fast spinning **BHs** can be observed in the inner regions of the $\alpha - \beta$ plane. The coordinate $|\alpha|$, the range of α values and (r, q) decrease (in magnitude) with the spin.

Parameter $\ell = \ell_\gamma^\pm$

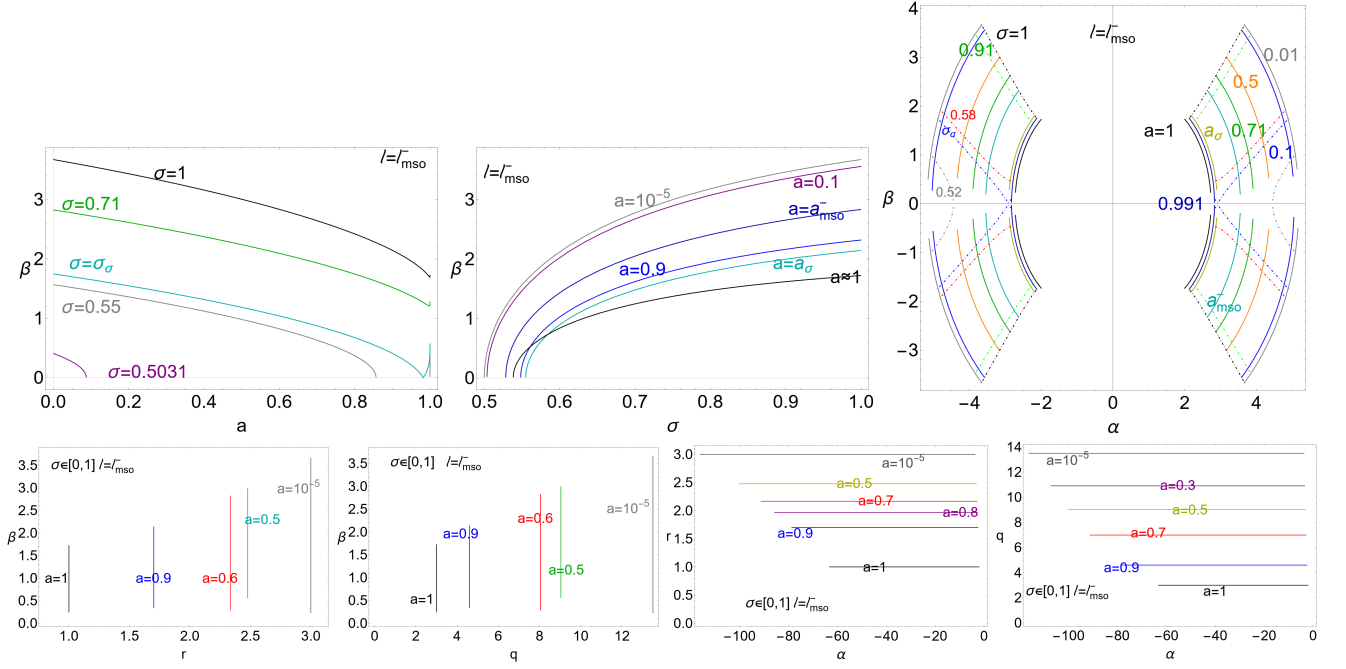


FIG. 5. Case $\ell = \ell_{mso}^-$. Upper panels: each point of a solid curve is for a different σ . Dotted-dashed lines are for different σ signed on the curves. Each point of a dotted-dashed curve is for a different spin a . Bottom panels: each point of a curve is for a different σ .

For $\ell = \ell_{\gamma}^{\pm}$ there are the photon circular orbits r_{γ}^{\pm} , on the equatorial plane, where $q = 0$ and $\sigma = 1$.

Parameter $\ell = \ell_{\mathbf{T}}$

The case of photons from the inversion surfaces, analyzed assuming $\ell = \ell_{\mathbf{T}}$, is shown in Figs (9) where $\beta(\alpha)$ for this impact parameter is shown at different σ and spin on the inversion surface, and the celestial coordinate β is then related to $(r_{\mathbf{T}}, \sigma_{\mathbf{T}})$. Figs (10) relate α to $(q, r_{\mathbf{T}}, \sigma_{\mathbf{T}})$, while $(r_{\mathbf{T}}, \sigma_{\mathbf{T}}, q, \ell)$ are analyzed in Figs (11,12). Within this constraint we consider $q \geq 0$, and $\dot{\phi} = 0$ for the inversion points i.e.

$$\mathcal{F}_{\mathbf{T}} \equiv a^2(\sigma - 1)\ell - 2ar\sigma - (r - 2)rl = 0. \quad (14)$$

There is $\alpha > 0$ since $\ell_{\mathbf{T}} < 0$, and in Figs (9) we restricted the analysis to $(\beta > 0, \alpha > 0)$. Note that for $\ell = \ell_{\mathbf{T}}$ function $\beta(\alpha)$ is strongly distinct from the case $\ell \in \{\ell_{mso}^{\pm}, \ell_{mbo}^{\pm}\}$ —see also Figs (3).

For fixed α , where $4.8 \lesssim |\beta| \lesssim 5.2$, the celestial coordinate $\beta(\alpha)$ decreases (in magnitude) with the **BH** spin. $|\beta|$ increases linearly with $r_{\mathbf{T}} > 2.5$, decreases with a for fixed $(\alpha, \sigma_{\mathbf{T}}, q)$, and it increases with $\sigma_{\mathbf{T}}$ and q (smaller values of q characterize fast spinning **BHs**). Considering Figs (10,11,12) for $\ell = \ell_{\mathbf{T}}$, quantity q , where $22 \lesssim q \lesssim 27$, increases with $|\alpha| < 2$. The coordinate β is maximum for $|\beta| \approx 5.196$ where $(r_{\mathbf{T}} = 3, q = 27)$ for $a = 1$ and $\sigma_{\mathbf{T}} = 1$. For $\sigma_{\mathbf{T}} \approx 0$ there is $(r_{\mathbf{T}} = 2.41421, |\beta| = 4.82843)$, there is $q = 22.31$ for $\sigma_{\mathbf{T}} \approx 0$ and $a = 1$.

Celestial coordinate $|\alpha|$ increases with q . Then, $|\alpha|$ (and α range) increases with a and $\sigma_{\mathbf{T}}$. Quantity q decreases in general with a and increases with $\sigma_{\mathbf{T}}$. Radius r increases with $(|\alpha|, \sigma_{\mathbf{T}}, q)$. However $r_{\mathbf{T}}$ decreases with a only for the limiting value $\sigma_{\mathbf{T}} \lesssim 0.63$ (related to the inversion surfaces maximum [94]).

Final remarks on the cases $\ell = \{\ell_{mbo}^{\pm}, \ell_{mso}^{\pm}, \ell_{\mathbf{T}}\}$

Figs (13), merging of Figs (5,6,7,8)—upper right panels, show cases $\ell = \{\ell_{mbo}^{\pm}, \ell_{mso}^{\pm}\}$. The shadow boundary regions correspondent to the inversion surfaces are completely distinct from the cases correspondent to $\ell = \{\ell_{mbo}^{\pm}, \ell_{mso}^{\pm}\}$. Furthermore, despite there is $\ell_{\mathbf{T}} < 0$, the shadows parts in the fast spinning **BHs** correspond to smaller values of $|\beta|$ (and larger range of $|\alpha|$).

Comparing profiles of Figs (5,6,7,8)—upper right panels and Figs (9, 13), it can be seen that in general, orbits for $\ell = \ell_{\mathbf{T}}$ are located approximately at the central region of the shadow boundary, ℓ_{mbo}^{\pm} is more external (larger values of α in magnitude), ℓ_{mso}^{\pm} is more internal.

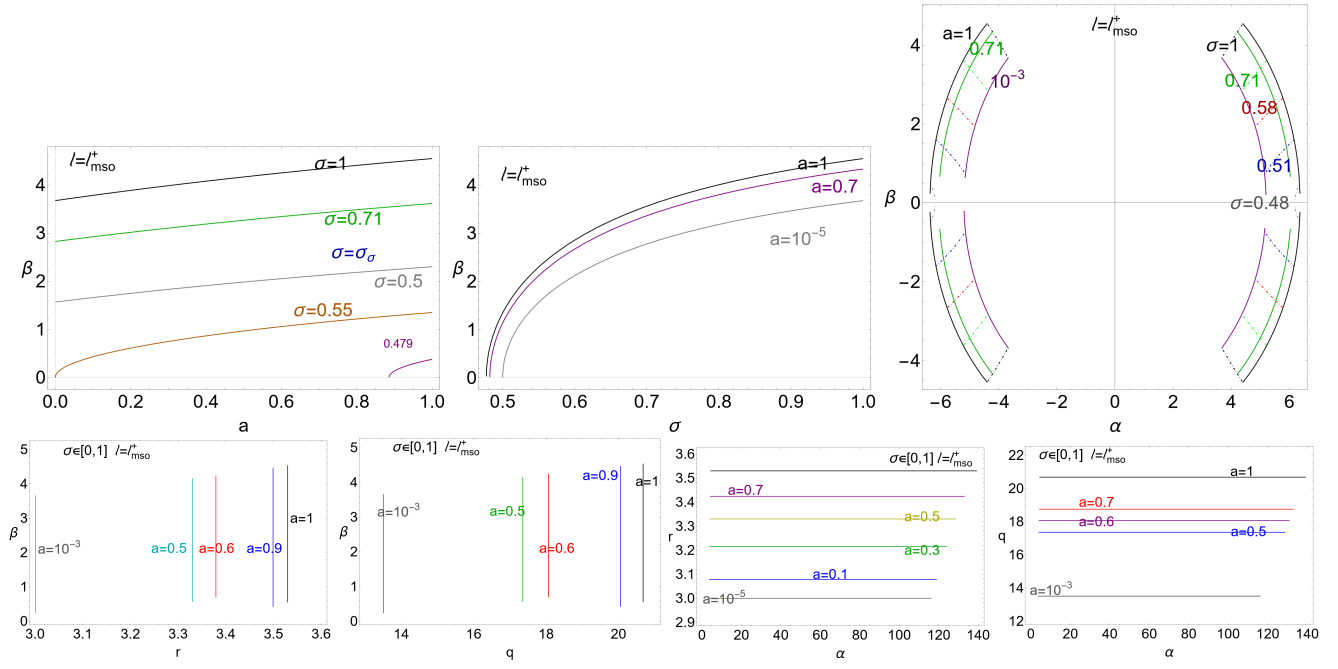


FIG. 6. Analysis of the $\ell = \ell_{mso}^+$ case. (For further details see Figs (5).)

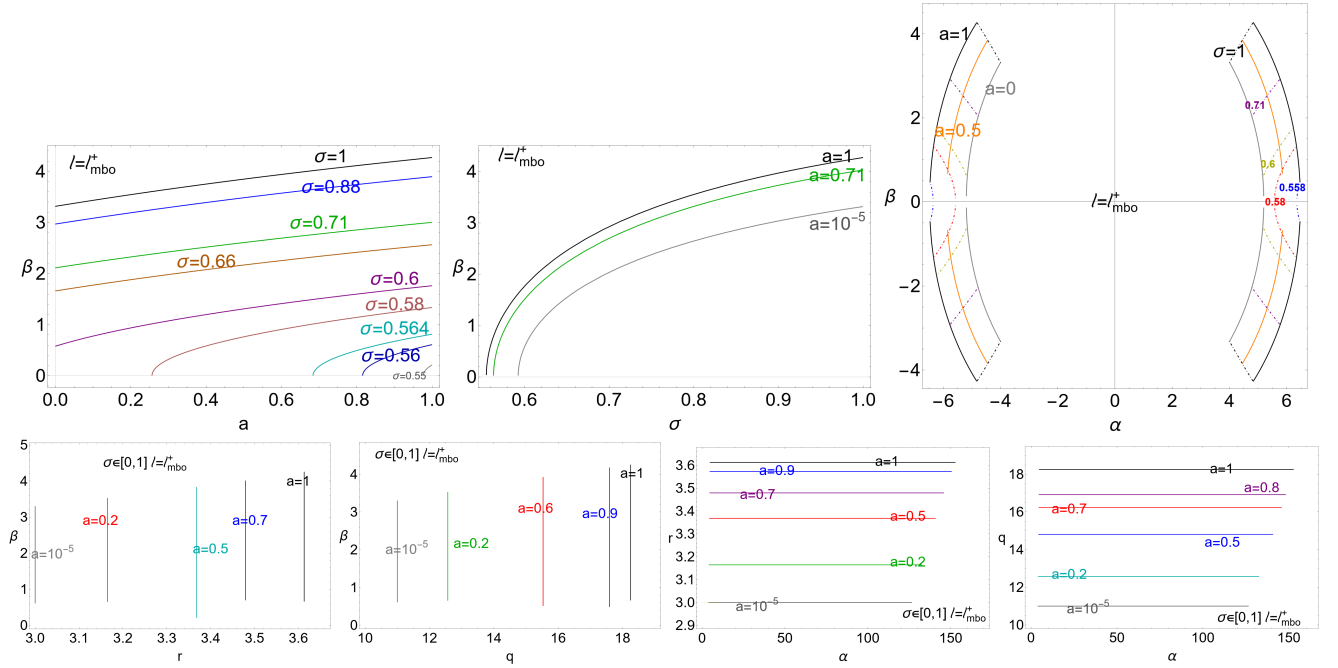


FIG. 7. Case $\ell = \ell_{mbo}^+$. (For further details see Figs (5).)

Analysis of σ_λ in Figs (4) shows that, for $\ell = \ell_{mso}^-$, the angle σ_λ increases with the **BH** spin a to the maximum value at $a = a_\sigma$. For $\ell = \{\ell_{mso}^+, \ell_{mbo}^+\}$, the angle σ_λ decreases with a and, for $\ell = \ell_{mbo}^-$, increases with a . There is

$$\sigma_\lambda(\ell_{mbo}^-) > \sigma_\lambda(\ell_{mbo}^+) > \sigma_\lambda(\ell_{mso}^-) > \sigma_\lambda(\ell_{mso}^+), \quad (15)$$

and in general $\sigma_\lambda \gtrsim 0.479$.

From Figs (2) it is noted that for $\sigma = 1$ coordinate α decreases (in magnitude) with the **BH** spin for the co-rotating

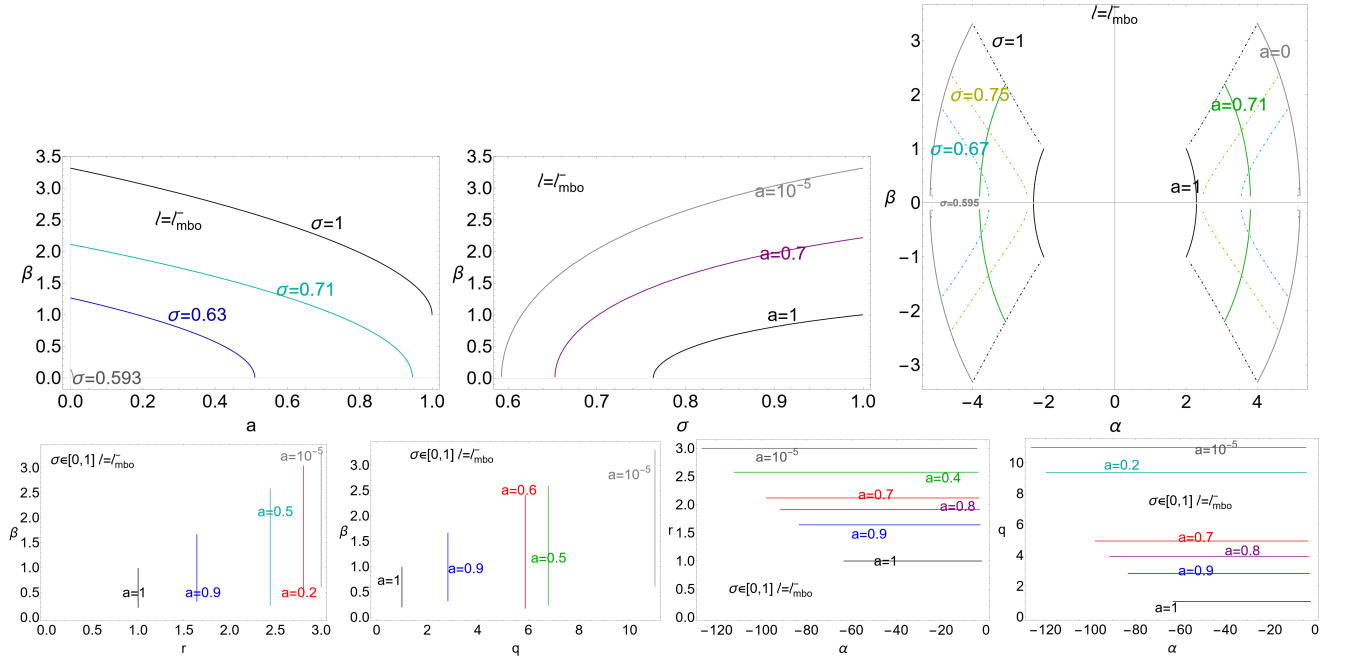


FIG. 8. Case $\ell = \ell_{mbo}^-$. (For further details see Figs (5)).

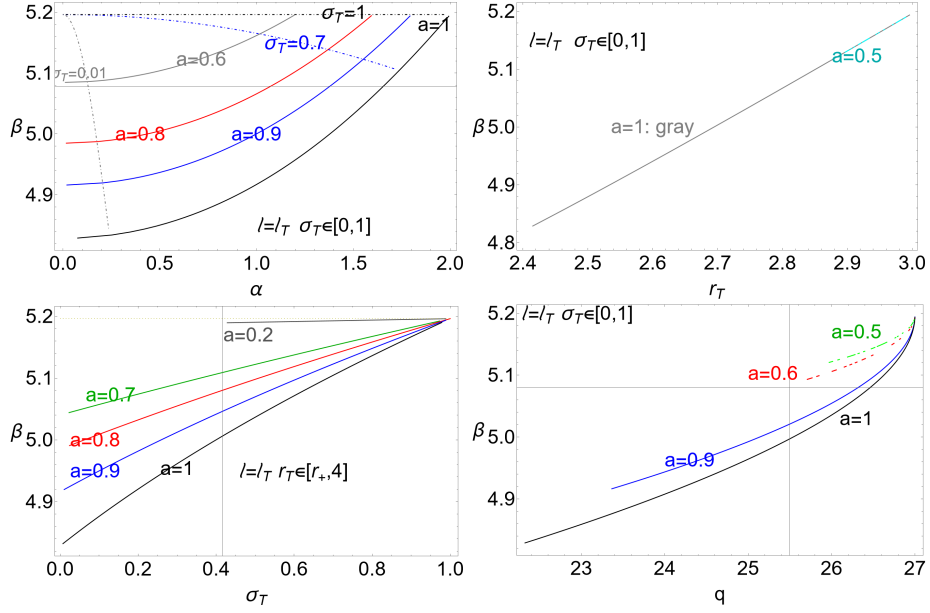


FIG. 9. Analysis for $\ell = \ell_{\mathbf{T}}$. Upper panels: each point of the solid curve is for a different angle $\sigma_{\mathbf{T}}$. Each point of a dotted-dashed curve is for a different a . As $\ell_{\mathbf{T}} < 0$, there is $\alpha > 0$, the analysis is for $(\beta > 0, \alpha > 0)$. Bottom left panel: each point of a curve is for a different radius $r_{\mathbf{T}}$. Bottom right panel: each point of each curve is for a different angle $\sigma_{\mathbf{T}}$.

cases and increases with spin for the counter-rotating case; there is

$$-\alpha_{\lambda}(\ell_{mso}^-) > -\alpha_{\lambda}(\ell_{mbo}^-) > -\alpha_{\lambda}(\ell_{\gamma}^-) \quad \text{and} \quad \alpha_{\lambda}(\ell_{\gamma}^+) > \alpha_{\lambda}(\ell_{mbo}^+) > \alpha_{\lambda}(\ell_{mso}^+). \quad (16)$$

On the other hand, q_{λ} increases with a for the counter-rotating cases and decreases with a in the co-rotating cases; there is

$$\begin{aligned} \text{for } a > a_q : \quad & q_{\lambda}(\ell_{mso}^+) > q_{\lambda}(\ell_{mbo}^+) > q_{\lambda}(\ell_{mso}^-) > q_{\lambda}(\ell_{mbo}^-), \quad \text{where } a_q \equiv 0.153054, \\ \text{for } a \in [0, a_q[: \quad & q_{\lambda}(\ell_{mso}^+) > q_{\lambda}(\ell_{mso}^-) > q_{\lambda}(\ell_{mbo}^+) > q_{\lambda}(\ell_{mbo}^-), \end{aligned} \quad (17)$$

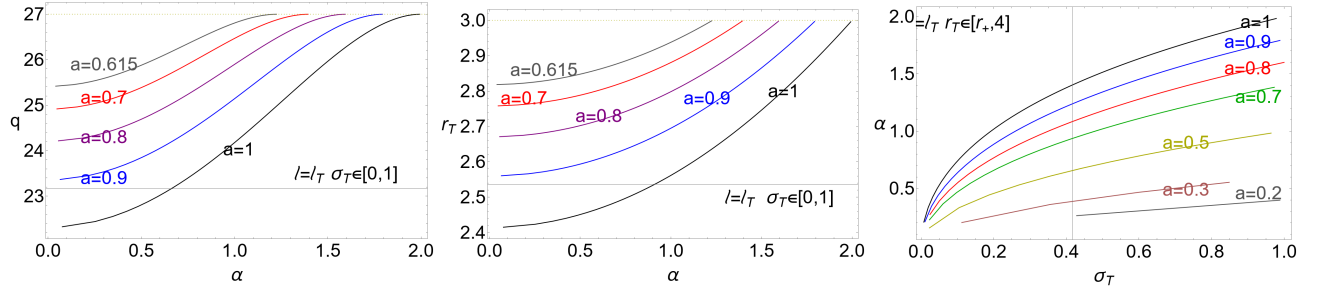


FIG. 10. Analysis for $\ell = \ell_T$. Left and center panels: each point of a curve is for a different σ_T . Right panel: each point of a curve is for a different radius r_T .

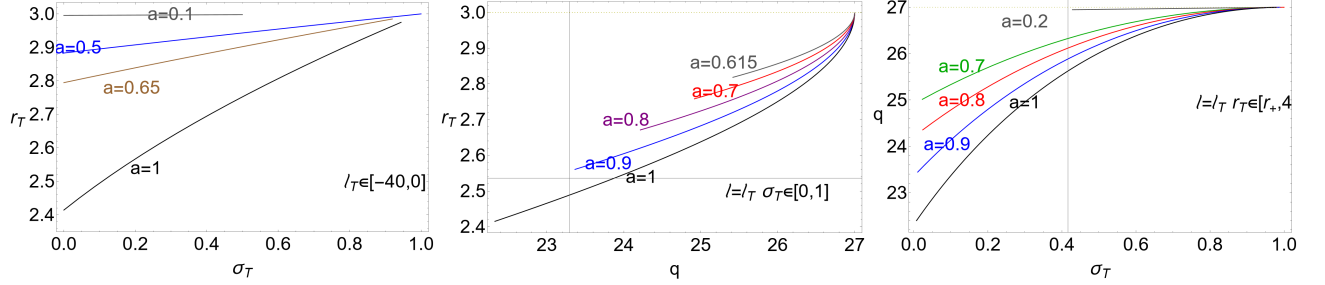


FIG. 11. Analysis for $\ell = \ell_T$. Left panel: each point of a curve is for a different ℓ_T . Center panel: each point of a curve is a different σ_T . Right panel: each point of a curve is a different radius r_T . For further details see also caption of Figs (10).

see Figs (2). From Figs (3) (and Figs (7)) it is clear that r_λ decreases with the **BH** spin for the co-rotating cases and it increases with the **BH** spin for the counter-rotating case. For $\ell \in \{\ell_{mbo}^+, \ell_{mso}^+\}$ there is $r_\lambda \in [r_\gamma^+, r_T(\sigma = 1)]$. However for $\ell = \ell_{mso}^-$ there is:

$$\text{for } a < a_\lambda^- : r_\lambda \in [r_\gamma^-, r_{mbo}^-], \quad \text{and for } a > a_\lambda^- : r_\lambda \in [r_{mbo}^-, r_{mso}^-]. \quad (18)$$

From Figs (13), showing the superimposition of the Figs (8,7,6,5)–right panels, it is possible to note that the **BH** spin is capable to distinguish the cases $\{\ell_{mbo}^\pm, \ell_{mso}^\pm\}$. For the static case ($a = 0$) the shadow boundary parts are very close and practically indistinguishable. The static case separates the co-rotating case (spread on the more internal and smaller region of the boundary–smaller values of $(|\alpha|, |\beta|)$) and the counter-rotating case (on a more external–larger values of $(|\alpha|, |\beta|)$) for different angles σ .

For an extreme Kerr **BH** there is

$$C_\beta(\ell_{mbo}^+) > C_\beta(\ell_{mso}^+) > C_\beta(\ell_{mso}^-) > C_\beta(\ell_{mbo}^-), \quad (19)$$

where $C_\beta(\ell_u) > C_\beta(\ell_v)$ indicates that the curve $C_\beta(\ell_u)$ for a momentum ℓ_u is more external (on the shadow boundary as in the Figs (13) than the curve $C_\beta(\ell_v)$ for a momentum ℓ_v , for different angles σ . Each curve has been evaluated

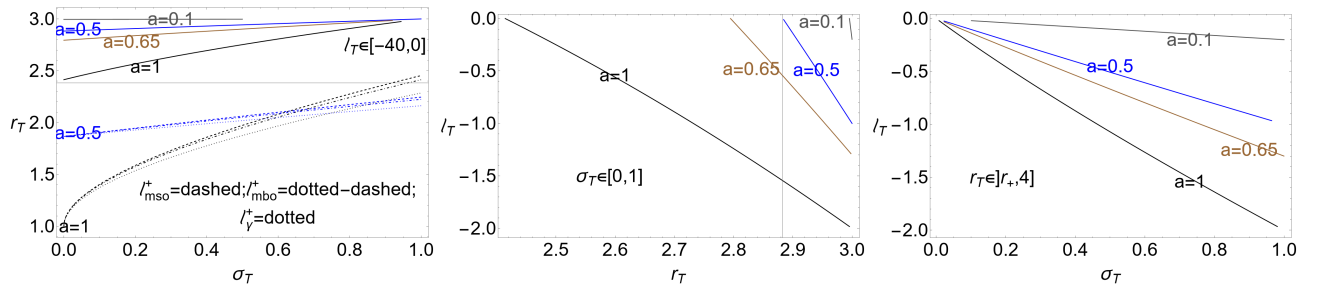


FIG. 12. Analysis for $\ell = \ell_T$. Left panel: each point is for a different ℓ_T . Middle panel: each point of a curve is for a different angle σ_T . Right panel: each point of a curve is for a different radius r_T . For further details see also caption of Figs (10).

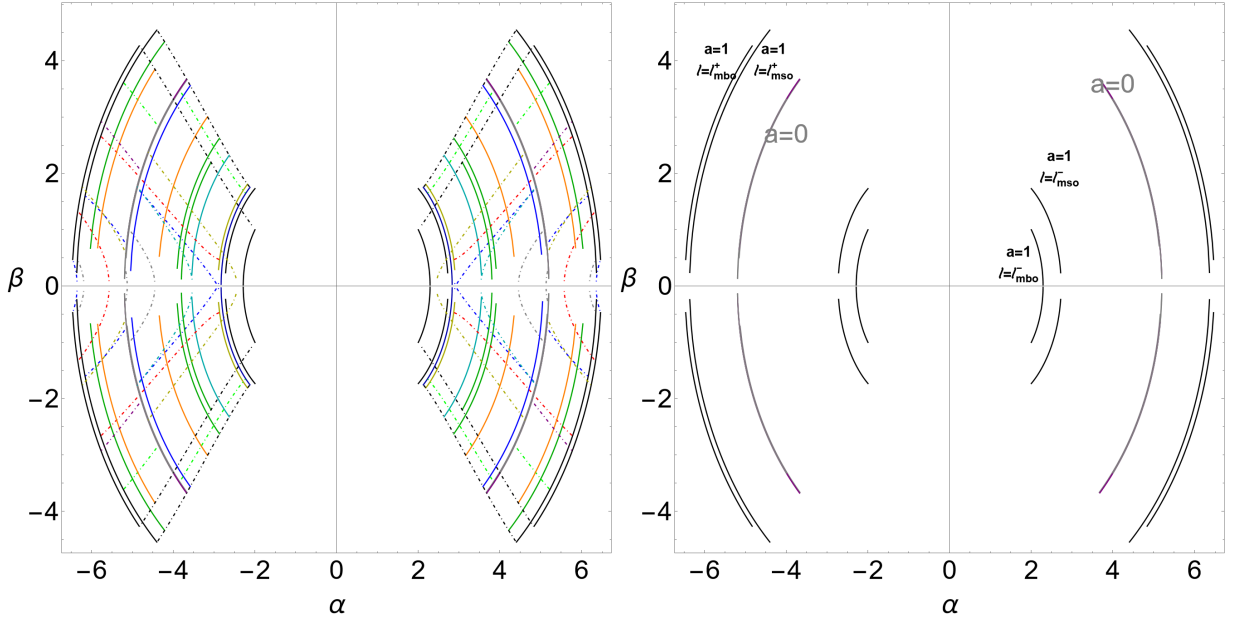


FIG. 13. Cases $\ell = \{\ell_{mbo}^{\pm}, \ell_{mso}^{\pm}\}$. Left panel: merging of Figs (8,7,6,5)–right panels. Dotted-dashed lines are for spin $a \in [0, 1]$ and for different angles σ . (Each point of a fixed curve is for a different spin a). Solid lines are for $\sigma \in [0, 1]$ and for different spin. (Each point of each curve is for a different angle σ). Right panel: each point of each curve is for a different angle σ .

for $\sigma \in [0, 1]$. Celestial coordinate $|\beta|$ increases generally for fixed α with the **BH** spin for the counter-rotating case and decreases with the **BH** spin for co-rotating case; α in magnitude increases for fixed β with the **BH** spin and the magnitude of ℓ^+ for the counter-rotating case, viceversa, α in magnitude decreases for fixed β with the **BH** spin and the ℓ^- for the co-rotating case. Whereby the co-rotating and counter-rotating cases are sharply distinct and distinguishable for each angle.

Note, from Figs (3) it is clear how in the co-rotating case r_{λ} can cross the outer ergosurface for fast spinning **BH**s (depending on the angle σ). We will focus on this special case in Sec. (IV C).

In general, considering r_{λ} as function of a , there is $r_{\lambda}^+ > r_{\lambda}^-$ for the counter-rotating and co-rotating cases. In the co-rotating case the radius r_{λ}^- decreases with the **BH** spin and there is $r \approx 3$ at $a \approx 0$. Viceversa r_{λ}^+ increases with the **BH** spin from $r \approx 3$ at $a \approx 0$ to $r \approx 4$ for $a \approx 1$. There is $r_{\lambda}^+(\ell_*^+) > r_{\Gamma}$ for $\ell_*^+ \in \{\ell_{mbo}^+, \ell_{mso}^+\}$ (see also Figs (3)) for any angle σ . Therefore photons from these inversion surfaces cannot be observed from the **BH** shadow boundary. However, as proved in this analysis, photons with $-\ell^+ = -\ell_{mso}^+$ can be part of the **BH** shadow boundary. Furthermore, there is

$$r_{\lambda}^+(\ell_{\gamma}^+) > r_{\lambda}^+(\ell_{mbo}^+) > r_{\lambda}^+(\ell_{mso}^+) > r_{\lambda}^-(\ell_{mso}^-) > r_{\lambda}^-(\ell_{mbo}^-) > r_{\lambda}^-(\ell_{\gamma}^-). \quad (20)$$

In Sec. (IV B) we analyze in additional details shadows from $r_{\lambda} \in \{r_{mbo}^-, r_{mso}^-\}$.

B. Assuming $r \in \{r_{mbo}^-, r_{mso}^-\}$

In general, photons spherical orbits, solutions of system (\mathfrak{R}) with $r_{\lambda} \in \{r_{mso}^{\pm}, r_{mbo}^{\pm}\}$, are for an impact parameter $\ell \neq \{\ell_{mso}^{\pm}, \ell_{mbo}^{\pm}\}$ and constant $q = q_{\lambda} \geq 0$. (The radius r_{λ} for $\ell \in \{\ell_{\gamma}^{\pm}, \ell_{mbo}^{\pm}, \ell_{mso}^{\pm}\}$ is compared in Figs (3) to the radii of the geodesic structures $r \in \{r_{\gamma}^{\pm}, r_{mbo}^{\pm}, r_{mso}^{\pm}\}$.) In this section we assume $r_{\lambda} \in [r_{mbo}^{\pm}, r_{mso}^{\pm}]$ and $r_{\lambda} \in [r_{\gamma}^{\pm}, r_{mbo}^{\pm}]$.

We will show that solutions of (\mathfrak{R}) for $r_{\lambda} \in [r_{mbo}^{\pm}, r_{mso}^{\pm}]$ and $r_{\lambda} \in [r_{\gamma}^{\pm}, r_{mbo}^{\pm}]$ are strongly differentiated. No solutions have been found for $r \in \{r_{mbo}^+, r_{mso}^+\}$, and we focus our study for $r \in \{r_{mbo}^-, r_{mso}^-\}$.

Case $r = r_{mso}^-$

From Figs (14) we see the situation for $r = r_{mso}^-$. There are solutions for co-rotating ($\ell > 0$) and counter-rotating ($\ell < 0$) photon orbits. Coordinate α is larger and positive for the counter-rotating case for $a \geq 0.66$. Coordinate $|\beta|$

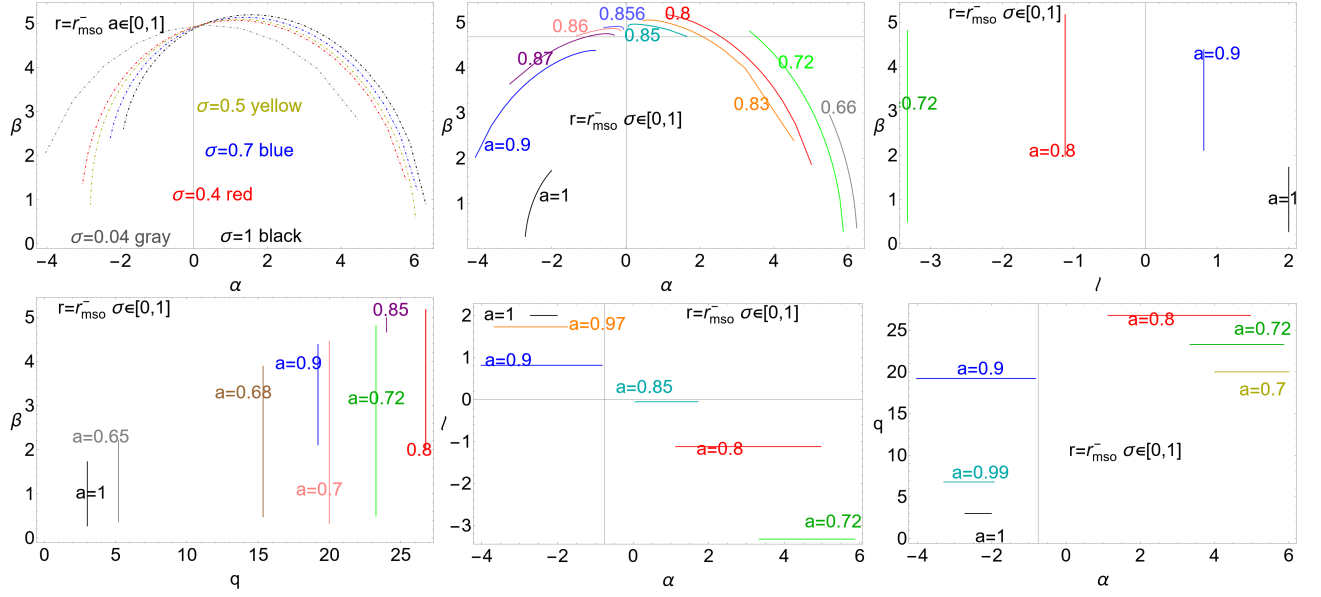


FIG. 14. Case $r = r_{mso}^-$. Each point of a curve is for a different σ . Upper left panel: each point of a curve is for a different a .

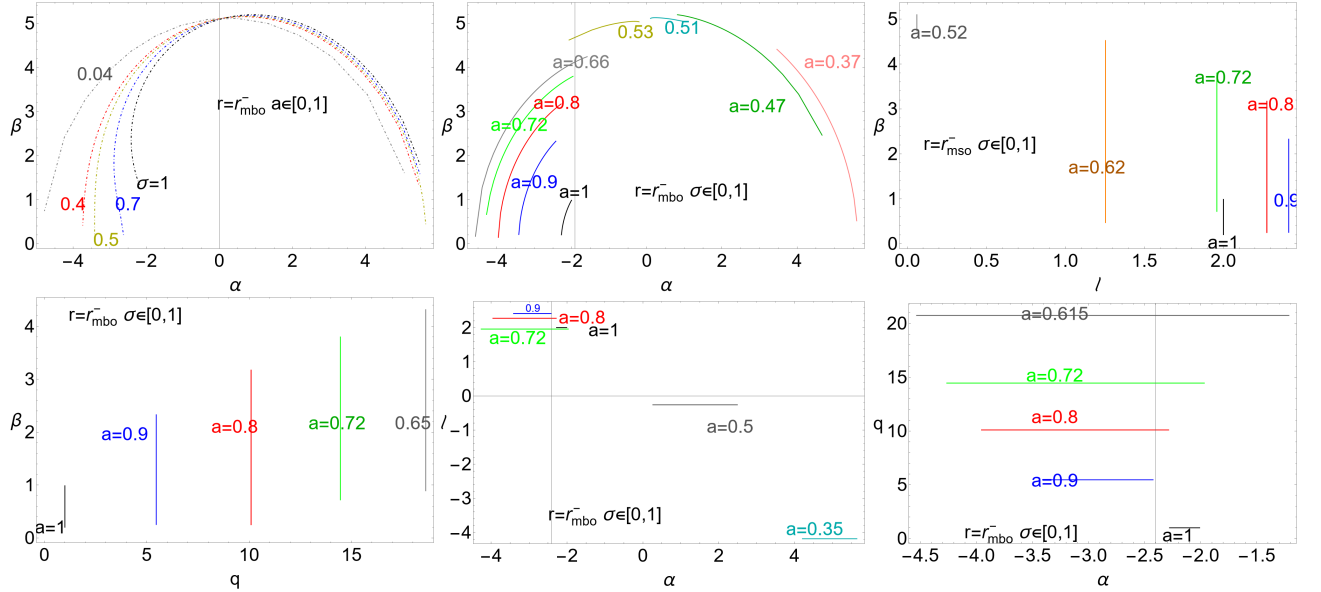


FIG. 15. Case $r = r_{mbo}^-$. (For further details see also caption of Figs (14).)

is larger for $a \approx 0.85$, and a minimum occurs for $a = 1$. $|\beta|$ is greater for ℓ small in magnitude, and it increases with q .

Case $r = r_{mbo}^-$

The case $r = r_{mbo}^-$ is shown in Figs (15) and it is qualitatively similar to the case $r = r_{mso}^-$.

In the spherical shells $[r_{mbo}^\pm, r_{mso}^\pm]$

In general, it can be $r_\lambda \in [r_{mbo}^\pm, r_{mso}^\pm]$ for some ranges of values of the impact parameter ℓ , and we study the general solutions: **(a)** $r_\lambda \in [r_{mbo}^+, r_{mso}^+]$, for $\ell < 0$ and **(b)** $r_\lambda \in [r_{mbo}^-, r_{mso}^-]$ for $\ell > 0$. It is convenient to consider the solution ℓ_λ of the equation $r = r_\lambda(\ell)$, leading to the impact parameter

$$\ell_\lambda \equiv \frac{a^2(r+1) + (r-3)r^2}{a(1-r)} : r_\lambda(\ell) = r, \quad (21)$$

showed in Figs (16) for different **BH** spin, with respect to the Kerr spacetime geodesic structure. Below we comment our results focusing first on the co-rotating case and we close this section with the analysis of the counter-rotating photons.

The co-rotating case

Momentum $\ell_\lambda > 0$ is shown (for $\sigma \in [0, 1]$) in Figs (16), with the limiting spins

$$a_{mso}^* \equiv 0.8528 : \ell_\lambda(r_{mso}^-) = 0, \quad a_{mbo}^* \equiv 0.516 : \ell_\lambda(r_{mbo}^-) = 0. \quad (22)$$

Assuming $\ell > 0$, there is $r_\lambda = r_{mso}^-$ for $a > a_{mso}^*$, and $r_\lambda = r_{mbo}^-$ for $a > a_{mbo}^*$, therefore in general $r \in [r_{mbo}^-, r_{mso}^-]$ only for $a > a_{mbo}^*$ (where $\sigma \in [0, 1]$), where further constraints should be applied, considering the full set of equations (5).

From Figs (3) it can be seen that $r_\lambda(\ell_{mso}^-) \in [r_{mbo}^-, r_{mso}^-]$ for $a > a_\lambda^-$.

More specifically, considering Figs (16) there is

$$\begin{aligned} \text{for } a \in [0, a_\lambda^-]: \quad & \ell_\gamma^- = \ell_\lambda(r_\gamma^-) > \ell_{mbo}^- > \ell_{mso}^- > \ell_\lambda(r_{mbo}^-) > \ell_\lambda(r_{mso}^-), \\ \text{for } a > a_\lambda^-: \quad & \ell_\gamma^- = \ell_\lambda(r_\gamma^-) > \ell_{mbo}^- > \ell_\lambda(r_{mbo}^-) > \ell_{mso}^- > \ell_\lambda(r_{mso}^-), \end{aligned} \quad (23)$$

for all $\sigma \in [0, 1]$. Hence, for $\ell > 0$, there is $r_\lambda \in [r_{mbo}^-, r_{mso}^-]$, with a momentum ℓ smaller then ℓ_{mso}^- for $a \in [0, a_\lambda^-]$. For $a > a_\lambda^-$ there is $r_\lambda \in [r_{mbo}^-, r_{mso}^-]$, close to r_{mbo}^- . (Radius r_λ is located in the ergoregion for sufficiently large spins.). Finally, according to the analysis of Fig. (17)-left panel, there is

$$C_\beta(r_{mbo}^-) > C_\beta(r_{mso}^-), \quad \text{for } \sigma = 1 \quad (24)$$

in the plane $\alpha - \beta$, in the sense that the curve correspondent to $r = r_{mbo}^-$ is more external then the curve for $r = r_{mso}^-$. As there is $\sigma = 1$, and therefore $\beta = \sqrt{q}$, solutions at $q = 0$ are only the curves $r = r_\gamma^-$.

From Figs (17)-right panel, we see that for fixed spin $a = 1$, radii r_{mso}^- and r_{mbo}^- are inside the outer ergoregion, and there are no solutions for a spin $a < a_{min}$ where, for r_{mso}^- , there is $a_{min} \approx 0.86$ (according to limit $a = a_{mso}^\lambda \equiv 0.7851 : r_\lambda(\ell_{mso}^-) = r_\epsilon^+$), for r_{mbo}^- there is $a_{min} = 0.66$, for r_ϵ^+ there is $a_{min} = 0.73$. Coordinate $|\beta|$ increases with σ . For large **BH** spins, curves for r_{mso}^- and r_{mbo}^- cross the ergosurface. (It is interesting to note that the ergosurfaces curves cross at different spins.). At fixed $r = r_{mso}^-$, the β variation with α distinguishes different **BH** spins. (In this analysis we selected the cases $\ell > 0$, therefore focusing on $\alpha < 0$). In this case, however, there is:

$$C_\beta(r_{mbo}^-) < C_\beta(r_{mso}^-), \quad \text{for } a \approx 1. \quad (25)$$

Figs (17)-left panel shows $\beta(\alpha)$ for all **BH** (dimensionless) spins $a \in [0, 1]$, for fixed orbits $r \in \{r_\epsilon^+, r_\gamma^\pm, r_{mso}^-, r_{mbo}^-, r_\tau, (r_\gamma^+ - 0.1)\}$ on the equatorial plane. Curves exist only for a spin $a > a_{min}$, in agreement also with the analysis of Figs (14) and Figs (15), where there is

$$\begin{aligned} \text{for } \sigma = 1: \quad & a_{min}(r_\gamma^-) \approx 0, \quad a_{min}(r_{mbo}^-) = 0.52, \quad a_{min}(r_{mso}^-) = 0.853, \\ & a_{min}(r_\gamma^+) \approx 0, \quad a_{min}(r_\tau) \approx 0, \quad a_{min}(r_\epsilon^+) = 0.71, \end{aligned} \quad (26)$$

–Fig. (17). Note, $a_{min}(r_{mbo}^-)$ corresponds to solution a_{mbo}^* , and $a_{min}(r_{mso}^-)$ to the limiting spin a_{mso}^* and $a_{min}(r_\epsilon^+)$ to $a_\gamma^\epsilon : r_\gamma^- = r_\epsilon^+(\sigma = 1)$. Finally, solutions with $\ell \in [\ell_{mbo}^-, \ell_\gamma^-]$ or $r_\lambda \in \{r_{mbo}^-, r_\gamma^-\}$ are also possible—see Figs (17).

In conclusion, the analysis on the co-rotating case shows that there are constraints on the spin and on the angle σ for the shadow boundary. The second condition explored here sees r_λ located in the orbital range for the accretion disk inner edge (or for cusps closer to the **BH**), addressed for larger poloidal angles and on the equatorial plane (where $q = 0$ only in the case of the photon circular orbit on the equatorial plane). In any case, there can be orbits on the outer ergosurface and in the outer ergoregion for fast spinning **BHs**—see Figs (3) and discussion in Sec. (IV C). However, this analysis proves that for any $\sigma \in [0, 1]$ there is (with small impact parameter) a bottom limit, (a_{min}, σ_{min}) , for the **BH** spin and the σ coordinate according to Eqs (22) and Eq. (26).

This implies that the contribution to the shadow boundary from co-rotating photons in the ranges considered here are constrained, especially for smaller σ and **BH** spins. Finally, we conclude by stressing that these orbital spherical shells can be in the **BH** ergoregion¹⁷ and in Sec. (IV C) we shall focus on shadows boundary from photons orbiting the outer ergosurface and the outer ergoregion.

¹⁷ For spin $a \in [a_{mbo}^\epsilon, a_{mso}^\epsilon[$ and will be in the ergoregion for spin $[a_{mso}^\epsilon, 1]$, where spins $\{a_\gamma^\epsilon, a_{mbo}^\epsilon, a_{mso}^\epsilon\}$ are in Figs (18)

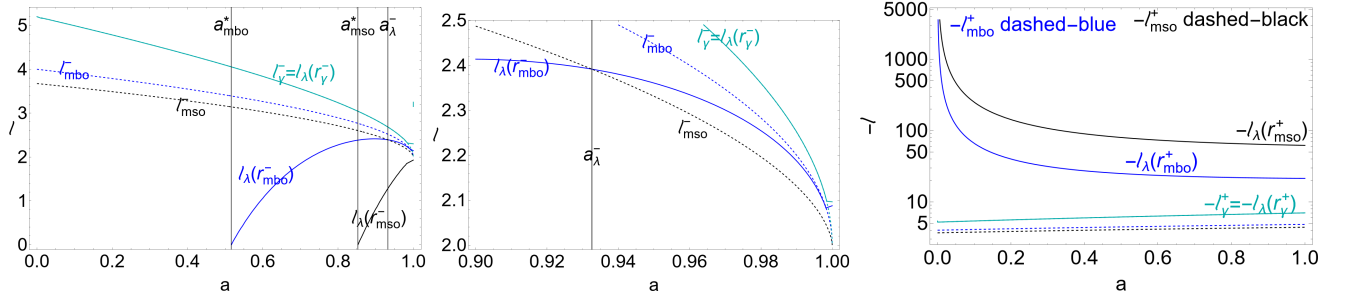


FIG. 16. Shadows from the inner edge (Sec. (IV B)). ℓ_λ is in Eq. (21). Left (right) panel shows the situation for the co-rotating (counter-rotating) case, center panel is a close-up of the left panel.

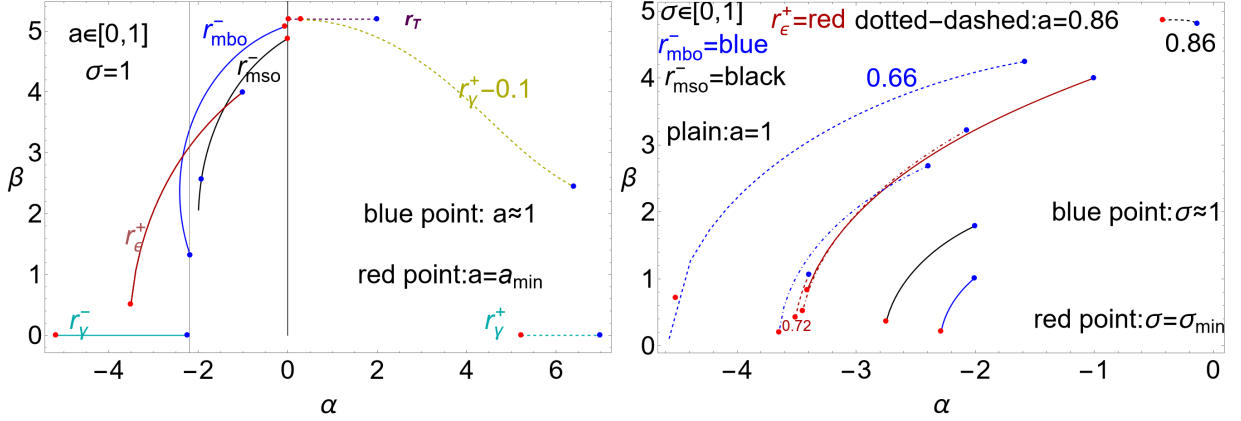


FIG. 17. Shadows from the inner edge (Sec. (IV B)). Left panel: there are no solutions for $r = \{r_{mso}^+, r_{mbo}^+\}$. Each point of a curve is for a spin a . a_{min} is the smallest **BH** spin a solution exists, different for each fixed radius r . Right panel: each point of a curve is for an angle σ . (It is $\ell > 0$ ($\alpha < 0$) for $\{r_{mso}^-, r_{mbo}^-, r_\gamma^-\}$ and $\ell < 0$ ($\alpha > 0$) for $\{r_{mso}^+, r_{mbo}^+, r_\gamma^+\}$). (Solutions $(-\alpha)$ are not represented).

The counter-rotating case

In the counter-rotating case the situation is strongly different. As clear from the analysis of Figs (7,6,2,4) there are solutions for $\ell \in \{\ell_{mso}^+, \ell_{mbo}^+\}$.

Considering Figs (16) we find that

$$-\ell_\lambda(r_{mso}^+) > -\ell_\lambda(r_{mbo}^+) > -\ell_\lambda(r_\gamma^+) = -\ell_\gamma^+ > -\ell_{mbo}^+ > -\ell_{mso}^+. \quad (27)$$

However, further inspection on the photons trajectories constraints informs that there are *no* counter-rotating solutions for $r > r_\gamma^+$. More generally, there is *no* solution $r_\lambda > r_\gamma^+$ for $\ell < 0$ (for *any* σ).

On the other hand, there is $r_\lambda < r_\gamma^+$ for $\ell \in \{\ell_{mso}^+, \ell_{mbo}^+\}$ that is, in this range of ℓ radius r_λ cannot be in the range for accretion disks inner edge on the equatorial plane.

Radius $r_\mathbf{T} < r_\gamma^+$ is shown, at any σ , in Figs (3). Figs (17)-left panel shows $\beta(\alpha)$ for all $a \in [0, 1]$ and for fixed orbits $r \in \{r_\epsilon^+, r_\gamma^\pm, r_{mso}^-, r_{mbo}^-, r_\mathbf{T}, (r_\gamma^+ - 0.1)\}$ on the equatorial plane (also for the counter-rotating orbits there is a bottom boundary (a_{min}, σ_{min}) for the **BH** spin and σ). If there is $\sigma = 1$, and therefore $\beta = \sqrt{q}$, solutions at $q = 0$ are only the orbits $r = r_\gamma^+$. Fig. (17) shows that on the equatorial plane the shadow from the inversion point, i.e. $r = r_\mathbf{T}$, is almost constant in α for different spins $a \in [a_{min}(r_\mathbf{T}), 1]$. It is also clear how the variation with spin for the curves $\beta(\alpha)$ is opposite for r_γ^- and r_γ^+ , and for r_ϵ^+ and $\{r_{mso}^-, r_{mbo}^-, r_\mathbf{T}, (r_\gamma^+ - 0.1)\}$ as β is greater for the fast spinning **BHs** and $|\alpha|$ is large for small spin. In the counter-rotating case, $|\beta|$ increases with decreasing r —Fig. (17).

The analysis of Figs (16) confirms the constraints on the specific angular momentum raising questions on the observability of the counter-rotating case as defined in this framework.

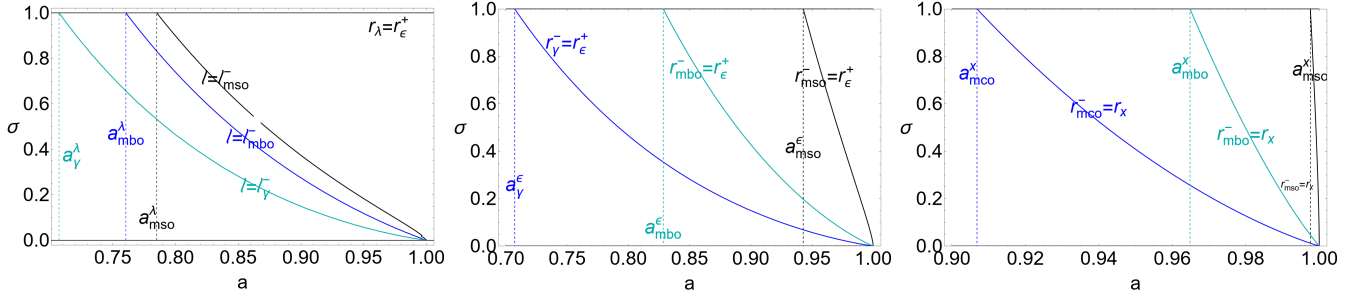


FIG. 18. Left panel: solutions $(\sigma, a) : r_\lambda(\ell_*) = r_\epsilon^+$, r_λ is in Eq. (12) and $\ell_* \in \{\ell_{mso}^-, \ell_{mbo}^-, \ell_\gamma^-\}$. For $\sigma = 1$ there is $r_\lambda(r_*) = r_\epsilon^+$ in the geometries with $a_* \in \{a_{mso}^\lambda, a_{mbo}^\lambda, a_\gamma^\lambda\}$ in Eqs (29). Center (right) panel: solutions $\sigma(a)$ of $r_\gamma^- = r_\epsilon^+(r_x)$, $r_{mbo}^- = r_\epsilon^+(r_x)$, $r_{mso}^- = r_\epsilon^+(r_x)$.

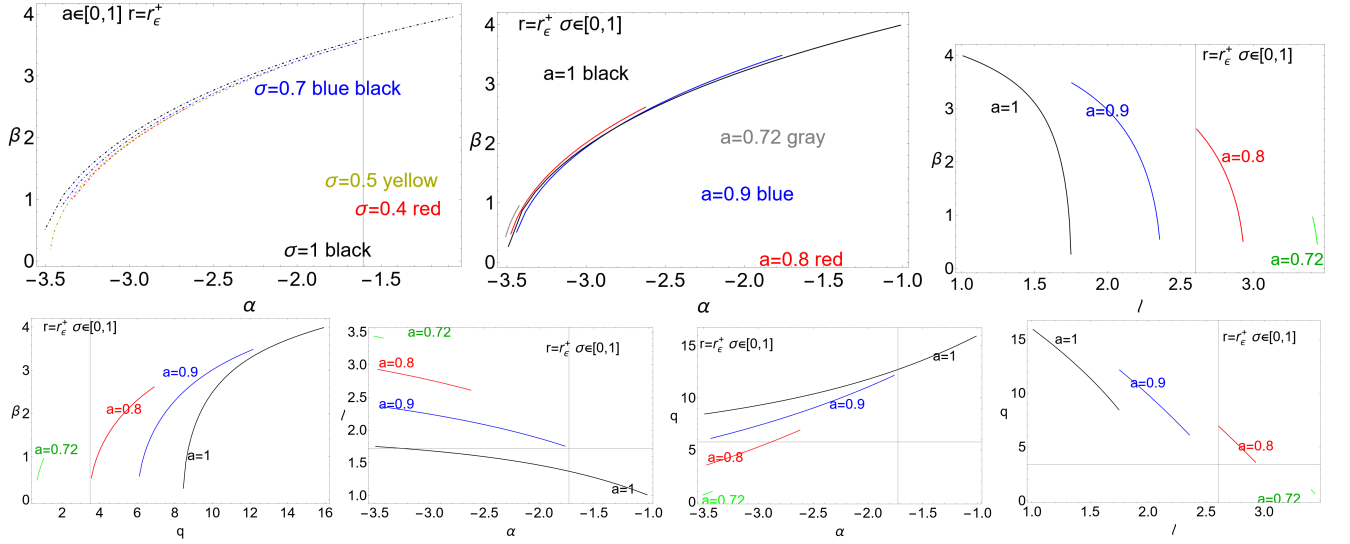


FIG. 19. Case $r = r_\epsilon^+$. Each point of a curve is for a different σ . Upper left panel: each point of a curve is for a different a .

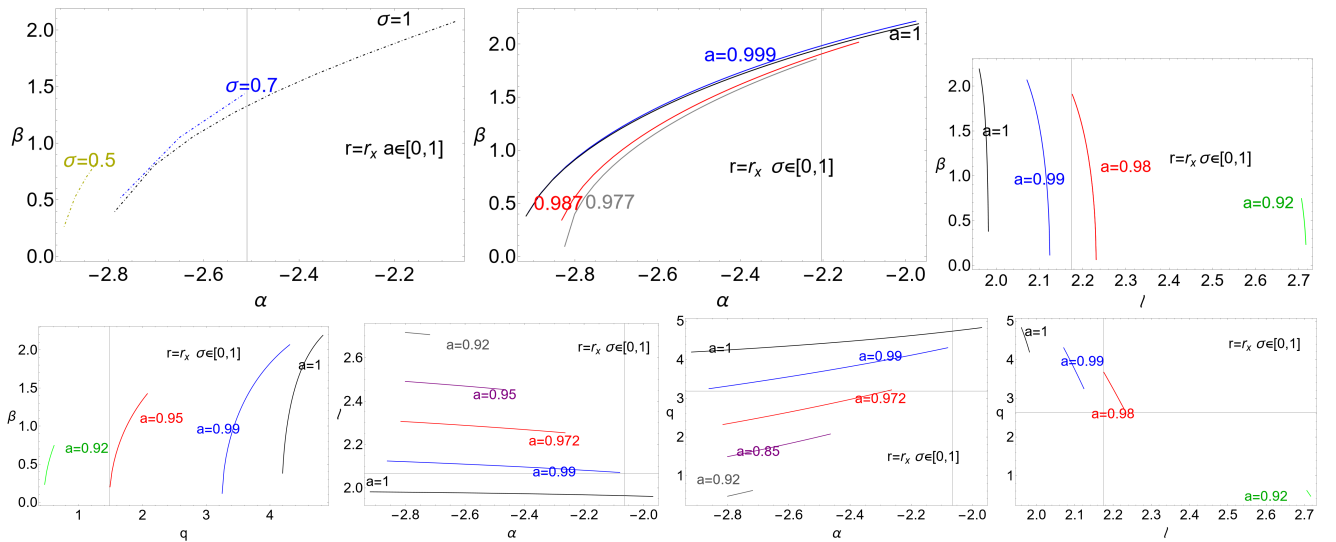


FIG. 20. Case $r = r_x \in]r_+, r_\epsilon^+[$ of Eq. (28). (For further details see also Figs (19).)

C. Shadows from the outer ergoregion

There can be stable, bound and unstable co-rotating circular orbits in the outer ergoregion of the fast spinning Kerr **BHs**. On the other hand, the inner edge of a co-rotating torus, are possible inside the ergoregion for large **BHs** spins [93]. In this section we consider the possibility that the outer ergoregion (and the outer ergosurface) will be “imprinted” in the shadow boundary, i.e. here we analyze solutions of the equations (\mathfrak{R}) for $r \in]r_+, r_\epsilon^+]$. First, from the analysis of Figs (3) it is clear, how (depending on the angle σ) in the co-rotating case, radius r_λ can cross the outer ergosurface for large **BH** spins.

Fig. (17) shows the shadow profiles from fixed orbits $r \in \{r_\epsilon^+, r_\gamma^\pm, r_{mso}^-, r_{mbo}^-, r_\mathbf{T}, (r_\gamma^+ - 0.1)\}$, on the equatorial plane $\sigma = 1$ for all **BH** spins $a \in [0, 1]$. (No counter-rotating solutions have been found for $r > r_\gamma^+$, and in particular for $r \in [r_{mso}^+, r_{mbo}^+]$).

The curve $\beta(\alpha)$, correspondent to the photons orbit coincident with the outer ergosurface ($r = r_\epsilon^+$), crosses the curve $\beta(\alpha)$ for fixed $r \in \{r_{mso}^-, r_{mbo}^-\}$ for determined values of α correspondent in general to different **BH** spins (each point of the curve represents a different spin, from a maximum $a = 1$, marked with a blue point, to a minimum a_{min} , different for each curve $\beta(\alpha)$ for fixed orbit r and marked with a red point). There is $a \in [a_{min}(r_\epsilon^+), 1]$ where $a_{min}(r_\epsilon^+) = 0.71$. Therefore, there is $r_\epsilon^+ \in [r_{mbo}^-, r_{mso}^-]$ only for some ranges of **BH** spins (in agreement with the analysis of Figs (3)). From Fig. (17) it is easy to see that, as there is $\sigma = 1$ and therefore $\beta = \sqrt{q}$, solutions at $q = 0$ are only the curves $r = r_\gamma^\pm$.

Therefore we set, at different angles $\sigma \in [0, 1]$, the condition $r = r_x \in]r_+, r_\epsilon^+[$ and $r = r_\epsilon^+$ respectively, where

$$r_x \equiv \frac{r_\epsilon^+ - r_+}{5} + r_+. \quad (28)$$

In Figs (19) the shadow boundary is shown for $r = r_\epsilon^+$, for different a and σ . The plots illustrate the dependence of the constrained coordinates β and α from parameters ℓ and q , and the curves $\ell(q)$ for $r = r_\epsilon^+$. The analysis of Figs (19) is reproduced in Figs (20) for $r = r_x$. In Figs (19,20), as $\ell > 0$ on $r = r_\epsilon^+$ and $r = r_x$, there is $\alpha < 0$, here we restricted the analysis to ($\beta > 0, \alpha < 0$).

From the outer ergosurface

Here we consider the case $r = r_\epsilon^+$.

From Figs (18)–left panel we see the solutions $(\sigma, a) : r_\lambda(\ell_*) = r_\epsilon^+$, for $\sigma \in [0, 1]$, and $\ell_* \in \{\ell_{mso}^-, \ell_{mbo}^-, \ell_\gamma^-\}$. For $\sigma = 1$ there is $r_\lambda(\ell_*) = r_\epsilon^+$ in the geometries with $a \geq a_*$ where $a_* \in \{a_{mso}^\lambda, a_{mbo}^\lambda, a_\gamma^\lambda\}$ defined as follows

$$\text{for } \sigma = 1 : \quad a_{mso}^\lambda \equiv 0.7851 : r_\lambda(\ell_{mso}^-) = r_\epsilon^+, \quad a_{mbo}^\lambda \equiv 0.76 : r_\lambda(\ell_{mbo}^-) = r_\epsilon^+, \quad a_\gamma^\lambda \equiv 0.7071 : r_\lambda(\ell_\gamma^-) = r_\epsilon^+, \quad (29)$$

radius $r_\lambda(\ell_*)$ for $\ell_* \in \{\ell_{mso}^-, \ell_{mbo}^-, \ell_\gamma^-\}$ is in the outer ergoregion in the geometries with **BH** spins $a \geq a_*$ where $a_* \in \{a_{mso}^\lambda, a_{mbo}^\lambda, a_\gamma^\lambda\}$ respectively, see Figs (18).

In Figs (18)–center and right panel we show the solutions $\sigma(a)$ of the equations $r_* = \{r_\epsilon^+, r_x\}$, where $r_* \in \{r_\gamma^-, r_{mbo}^-, r_{mso}^-\}$. It is convenient to introduce the spins

$$a_{mbo}^\epsilon \equiv 0.828427 : r_{mbo}^- = r_\epsilon^+(\sigma = 1), \quad a_\gamma^\epsilon \equiv 0.707107 : r_\gamma^- = r_\epsilon^+(\sigma = 1), \quad a_{mso}^\epsilon \equiv 0.942809 : r_{mso}^- = r_\epsilon^+(\sigma = 1), \quad (30)$$

similarly spins $\{a_\gamma^x, a_{mbo}^x, a_{mso}^x\}$ are defined by $r_* = r_x(\sigma = 1)$ –see Figs (18). Note, in general $\{a_{mso}^\lambda, a_{mbo}^\lambda, a_\gamma^\lambda\}$ do not coincide with spins $\{a_{mso}^\epsilon, a_{mbo}^\epsilon, a_\gamma^\epsilon\}$ (both defined for $\sigma = 1$) in Eq. (30). However, there is $a_\gamma^\lambda = a_\gamma^\epsilon$.

Results of this analysis are shown in Figs (19,20): we note that the coordinate $|\beta|$ decreases with ℓ and $|\alpha| < 3.5$, and increases with $q \lesssim 16$. At fixed α , it decreases with a and increases with σ . Quantity q decreases with α in magnitude, $|\alpha|$ increases with ℓ and decreases with q .

From the outer ergoregion

A qualitatively similar situation occurs for a point $r = r_x$, located inside the outer ergoregion–Figs (20)–but with some notable differences with respect to the orbits from the outer ergosurface. In Figs (21) there are the shadows boundaries for different (a, σ) for $\ell = \{\ell_{mbo}^\pm, \ell_{mso}^\pm, \ell_\mathbf{T}\}$ and $r = \{r_\epsilon^+, r_x\}$, (merging of Figs (5,6,7,8,13)–upper right panles). The analysis in Figs (21) allows to clarify how the situation for photons orbiting in the ergoregion, at $r_\lambda = r_x$, appears different as compared to $r_\lambda = r_\epsilon^+$. At $a = 1$, the curve $\beta(\alpha)$ at $r_\lambda = r_\epsilon^+$ is more external than the curve at $r_\lambda = r_x$ (in agreement with the situation for the other curves $\beta(\alpha)$).

However, differences appear with the variation of the **BH** spin at fixed radius r_λ . For $r_\lambda = r_\epsilon^+$, the curve moves inward with increasing of the **BH** spin, viceversa the curve corresponding to the orbits at $r_\lambda = r_x$ moves inward

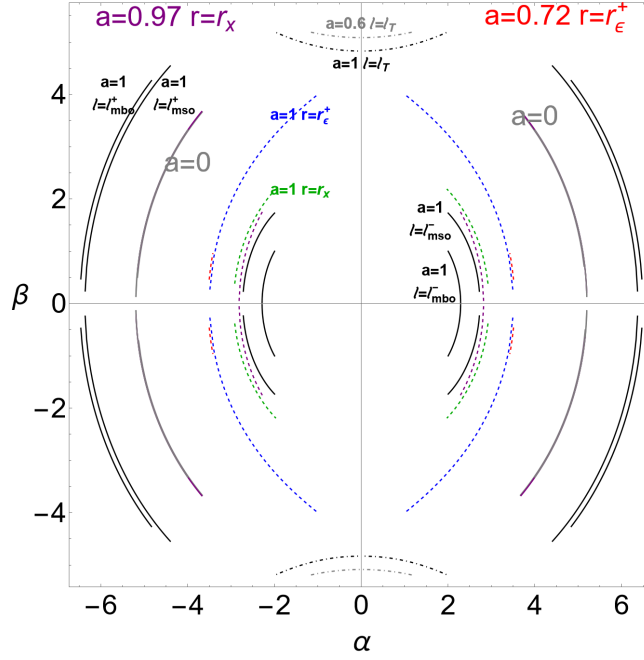


FIG. 21. Cases $\ell = \{\ell_{mbo}^{\pm}, \ell_{mso}^{\pm}, \ell_{\mathbf{T}}\}$ and $r = \{r_{\epsilon}^+, r_x\}$, merging of Figs (13,8,7,6). Each point of a curve is for a different value of σ .

with decreasing of the **BH** spin in contrast with the other curves for the co-rotating orbits. (We remind that r_x is a function of (a, σ)). This divergence appears also from the comparison of Figs (20) and Figs (19), also for the curve $\beta(\alpha)$ at different **BH** spin for a fixed angle.

Therefore, orbits in the outer ergosurface and the outer ergoregion are possible for **BH** spin $a > a_{min}$ and $\sigma \in [\sigma_{min}, 1]$, where the σ are explored in Figs (17) and the limits for a general ℓ are in Figs (19,18,20). In general $|\beta|$ is greatest for $\sigma = 1$. Figs (22) show the location of the photons considered in this analysis (cases $\ell = \{\ell_{mbo}^{\pm}, \ell_{mso}^{\pm}, \ell_{\mathbf{T}}\}$ and $r = \{r_{\epsilon}^+, r_x\}$) on the **BH** shadow boundary, for selected values of (a, σ) , complementing the analysis of Sec. (IV A).

Figs (21) show cases $\ell = \{\ell_{mbo}^{\pm}, \ell_{mso}^{\pm}, \ell_{\mathbf{T}}\}$ and $r = \{r_{\epsilon}^+, r_x\}$. Curves at $\{\ell_{mbo}^-, \ell_{mso}^-\}$ are inside the outer ergoregion. There is

$$C_{\beta}(a = 0.72, r_{\epsilon}^+) < C_{\beta}(a = 1, r_{\epsilon}^+) < C_{\beta}(a = 1, r_x) < C_{\beta}(a = 0.97, r_x) < C_{\beta}(a = 1, \ell_{mso}^-) < C_{\beta}(a = 1, \ell_{mbo}^-) \quad (31)$$

where $C_{\beta}(\mathbf{Y}) > C_{\beta}(\mathbf{Z})$ indicates that the curve $C_{\beta}(\mathbf{Y})$ for a parameter set \mathbf{Y} is more external (on the shadow boundary as in the Figs (21)) than the curve $C_{\beta}(\mathbf{Z})$ for the set of parameters \mathbf{Z} , for different $\sigma \in [0, 1]$.

Therefore, at fixed spin, the curve of the plane $\alpha - \beta$, from orbits from the outer ergosurface, is more external than the curve correspondent to photon orbits r_x inside the ergoregion. On the outer ergosurface, as for the other cases with fixed $\ell > 0$, the largest **BH** spins correspond to innermost curves of the plane $\alpha - \beta$. Viceversa, in agreement with the analysis in Figs (20), inside the ergoregion (on the orbit r_x), the fast spinning **BH**s correspond to outer curves in the $\alpha - \beta$ plane.

V. DISCUSSION AND CONCLUSIONS

Co-rotating and counter-rotating null geodesics, solutions of set (\mathfrak{R}) in Eqs (9) have been constrained by their impact parameter ℓ or radii r , and related to particular parts of the shadow boundary. Hence, as results we obtained a map, for all (σ, a) , of regions on the shadows boundaries, correspondent to photon spherical orbits with $\ell \in \{\ell_{\mathbf{T}}(a), \ell_{mso}^{\pm}(a), \ell_{mbo}^{\pm}(a), \ell_{\gamma}^{\pm}(a)\}$, or with radius r in the outer ergoregion, $r \in [r_+, r_{\epsilon}^+]$, in the spherical shells and on the spherical surfaces defined by the radii $r = \{r_{mso}^{\pm}, r_{mbo}^{\pm}, r_{\gamma}^{\pm}\}$. Results are illustrated in Figs (22) (for fixed angle σ and spin a), in Figs (21) and Figs (13,8,7,6,5)—upper right panels (for all angles σ and spin a).

Note, fixing (a, σ) , solutions of (\mathfrak{R}) with fixed ℓ or r , are a set of points on the shadow boundary represented by the vertical lines in the plane $\alpha - \beta$ of Figs (22).

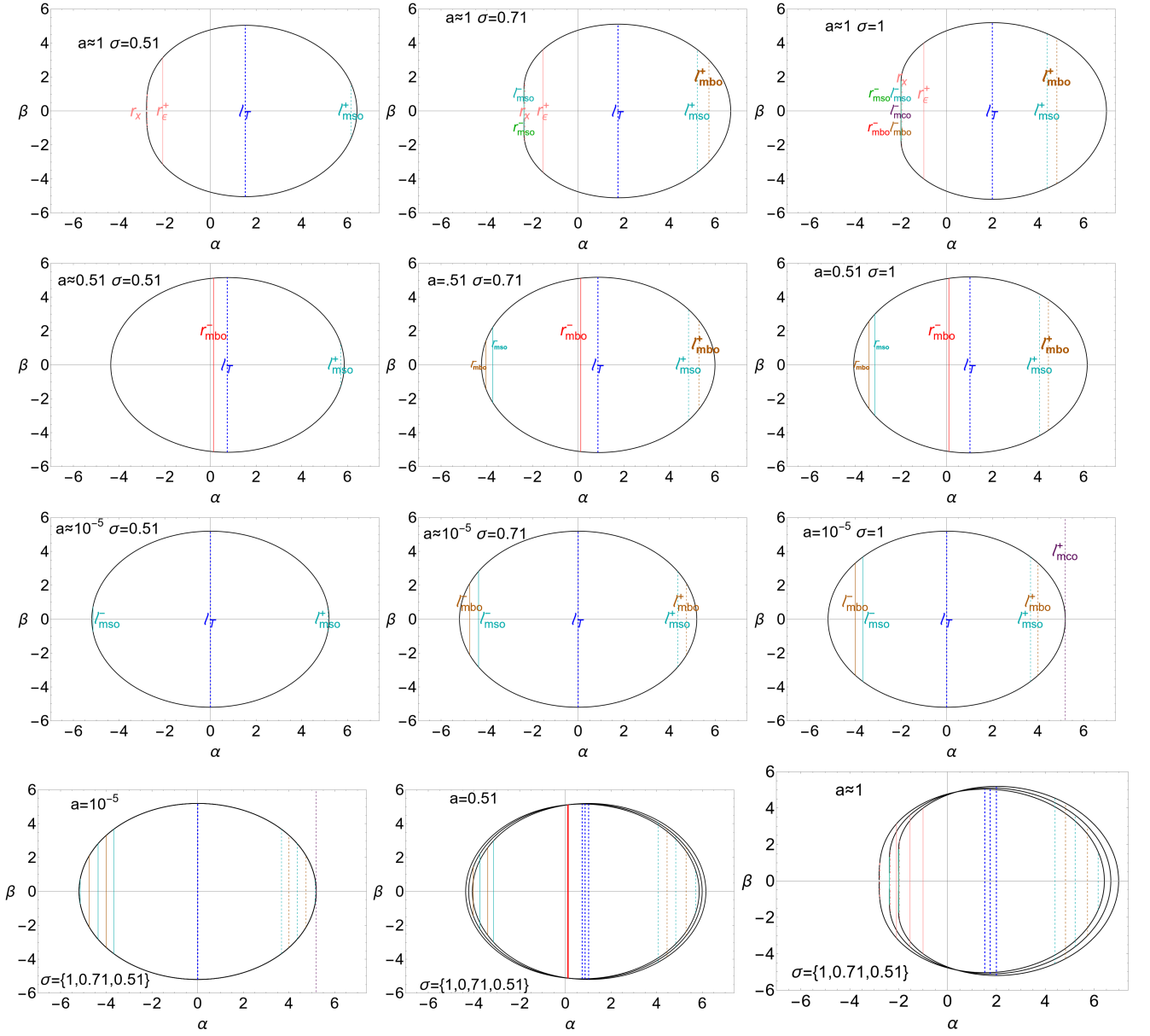


FIG. 22. Boundary of the **BH** shadows. Dashed blue vertical lines are $\ell = \ell_{\mathbf{T}}$. Vertical orange, purple and cyan lines are $\ell \in \{\ell_{mbo}^{\pm}, \ell_{\gamma}^{\pm}, \ell_{mso}^{\pm}\}$ respectively. (Pink solid, pink dotted-dashed, red, green) lines are for $r = \{r_{\epsilon}^+, r_x, r_{mbo}^-, r = r_{mso}^-\}$. ($-\alpha$) for simplicity have been omitted here).

On the other hand, solving (\mathfrak{R}) with constraints on ℓ or r , at *fixed* a and for *all* $\sigma \in [0, 1]$, provides *curves* of the $\alpha - \beta$ plane, made of points of the shadow boundaries relative to the constrained null spherical geodesics, for *all* values of σ . The results of this analysis are shown in Figs (21,13), and as solid curves of Figs (8,7,6,5)–upper right panels. In these plots each solid curve corresponds to a *fixed* spin, and each point of each solid curve is for *fixed* σ . Dotted–dashed lines are for a fixed σ , and each point of a dotted–dashed line is for a different spin. Then (α, β) have been then directly related, for each constraint, to the quantities (a, σ, r, ℓ, q) in Figs (10,11,12) and Figs (13,8,7,6,5).

Findings for photons spherical orbits in the outer ergoregion are shown in Figs (19,20,21) and discussed in Sec. (IV C). The possibility to observe the emission from the outer ergosurface and from the inside the outer ergoregion is limited for **BH** spin $a > a_{min}$ as from a angle $\sigma \in [\sigma_{min}, 1]$ (in general $|\beta|$ is greater for $\sigma = 1$) where (a_{min}, σ_{min}) have been discussed in Sec. (IV C)–see also Figs (22).

In general there are solutions for parameters $\ell \in \{\ell_{mso}^+, \ell_{mbo}^+, \ell_{\gamma}^+, \ell_{\mathbf{T}}\}$ –see for example Figs (6,7)–, while no solutions have been found for $r \in \{r_{mbo}^+, r_{mso}^+\}$ –Sec. (IV B).

Figs (13) and Figs (21) summarize results showing the difference between the co-rotating and counter-rotating

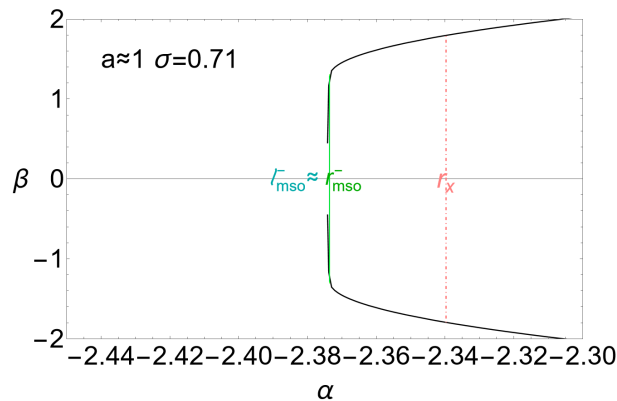


FIG. 23. A close view of the case ($a \approx 1, \sigma = 0.71$) in Fig. (22).

photon orbits considered within the different constraints, at different (a, σ).

Results for $\ell = \ell_{mso}^-$ are in Figs (5), solutions are $\sigma \gtrsim 0.53$ and β (in magnitude) increases with σ and decreases with a for $\sigma < \sigma_\sigma$ and $a < a_\sigma$ —Figs (4)). Differently for $\sigma > \sigma_\sigma$, and $\sigma \in [0.53, \sigma_\sigma]$. With ($\sigma > \sigma_\sigma, a > a_\sigma$), solutions appear for small values of (β, α) in magnitude, distinguishing slower from faster spinning **BHs**, and the smaller ($\sigma \approx 0.56$) from larger σ .

Photons with $\ell = \ell_{mso}^+$ are considered in Figs (6). Inner regions of the $\alpha - \beta$ plane, characterize slowly spinning **BHs**. $|\beta|$ increases with the **BH** spin and the angle $\sigma > 0.479$. For $\sigma > 0.55$ there is $|\beta| > 0$. The case $\ell = \ell_{mbo}^-$ is in Figs (8) and the results for $\ell = \ell_{mbo}^+$ are for Figs (7). ($\ell = \ell_\gamma^\pm$ correspond to photon circular orbits r_γ^\pm , on the equatorial plane ($q = 0$)). The case of photons from the inversion surfaces, is shown in Figs (9,10,11,12). Solutions of (\mathfrak{R}) for $r_\lambda \in [r_{mbo}^\pm, r_{mso}^\pm]$ and $r_\lambda \in [r_\gamma^\pm, r_{mbo}^\pm]$ are strongly differentiated and there are no solutions have been found for $r \in \{r_{mbo}^+, r_{mso}^+\}$. The case $r = r_{mbo}^-$ is shown in Figs (15). Case $r = r_{mso}^-$ is in Figs (14 for co-rotating and counter-rotating photon orbits. Orbits in the shell $r_\lambda \in [r_{mbo}^+, r_{mso}^+]$ are studied for $\ell < 0$ and $\ell > 0$ for $r_\lambda \in [r_{mbo}^-, r_{mso}^-]$ only for $a > a_{mbo}^*$, in fact we found solutions on $r_\lambda = r_{mso}^*$ for $a > a_{mso}^*$, and on $r_\lambda = r_{mbo}^*$ for $a > a_{mbo}^*$. On the other hand, from Figs (3) it can be seen that $r_\lambda(\ell_{mso}^-) \in [r_{mbo}^-, r_{mso}^-]$ for $a > a_\lambda^-$. As clear from the analysis of Figs (7,6,2,4), there are solutions for $\ell \in \{\ell_{mso}^+, \ell_{mbo}^+\}$. There are *no* counter-rotating solutions for $r > r_\gamma^+$.

The poles ($\sigma \approx 0$) and the ergoregion of a Kerr **BH**, explored in this work, are regions where it would be possible to trace important information on the spacetime structure for these **BHs** and the processes involving fields and matter constituting the astrophysical **BH** embedding environment. We stress that realistic **BH** shadows can depend on properties of the region of the light distribution and its source, as the accretion disks, with photons interacting with the accreting plasma. **BH** shadow may also be affected by physical processes involving the accreting disk inner edge¹⁸.

We expect that the regions highlighted here will be distinctly recognizable in future observational enhancement. **EHT** Collaboration has already compared numerical torus models directly to observations in several comprehensive analyses, performing **GRMHD** models fit with the observations¹⁹, for example in [5, 14]. For this reason there is no

¹⁸ Disk inner edge location is not fixed in time but can move inward, towards the central **BH**, or outward as, for example, in the runaway instability [24, 26, 51, 56, 66], or due to establishment of successive, interrupted, accretion phases modelling different phases of super-Eddington accretion—see for example [27, 61, 68, 84, 109–111]. The inner regions of the accretion disks are also characterized by oscillations and modes, as quasi-periodic oscillations. A further interesting aspect to consider in this frame would be to **BH** shadows following a spin variation (precession) process, for tori not located in the equatorial plane of the central **BH** [29, 47, 52, 63–65, 69, 71, 76, 78, 79, 81–83, 98].

¹⁹ Various **GRMHD** analyses have been implemented to **EHT** images interpretation in [4, 6] and especially in [5]—see also [54, 55, 60, 80, 87], investigating the origin of the photons forming the **EHT** image at base of the **M87** jet and disk—[5, 87]. An analytic disk model has been also developed in [108] for the **M87*** accretion flow, computing the synchrotron emission from the disk model assuming different spacetimes, and numerical fits to the **EHT** data. **GRMHD** simulations with jet ejection and accretion flows simulated from first principles were in [18] with the **EHT** observations of the jet launching and collimation in Centaurus **A** (see [44]). In [45] **EHT** images were analysed and interpreted by **GRMHD** models of tilted accretion discs, finding that **M87** may feature a tilted disc/jet systems—see also [2, 112]. In [30] there are **GRMHD** simulations of novel models for high-energy particles in systems of jet/accretion flow with emission of synchrotron radiation. Vast simulations of different accretion models were provided in [5, 14] and simulations of both thick torii and thin disks and different implementations of the interaction between radiation and the plasma fluid are in [20, 45]. [8] focused on description of the polarimetric observations and the relativistic jet, using a large library of simulated polarimetric images from **GRMHD** simulations. (Magnetically arrested accretion disks were considered as consistent **GRMHD** models.). Numerical

fixing accretion or accretion disk model. In this sense our analysis can be adaptable to and complement the constraints imposed by the specific numerical or analytical model of accretion disks.

DATA AVAILABILITY

There are no new data associated with this article. No new data were generated or analysed in support of this research.

-
- [1] Akiyama K. et al. (Event Horizon Telescope), 2019a, *Astrophys. J.*, 875, L1
 - [2] Akiyama K. et al. (Event Horizon Telescope), 2019b, *Astrophys. J.*, 875, L2
 - [3] Akiyama K. et al. (Event Horizon Telescope), 2019c, *Astrophys. J.*, 875, L3
 - [4] Akiyama K. et al. (Event Horizon Telescope), 2019d, *Astrophys. J.*, 875, L4
 - [5] Akiyama K. et al. (Event Horizon Telescope), 2019e, *Astrophys. J.*, 875, L5
 - [6] Akiyama K. et al. (Event Horizon Telescope), 2019f, *Astrophys. J.*, 875, L6
 - [7] Akiyama K. et al. (Event Horizon Telescope), 2021a, *ApJL*, 910, L12
 - [8] Akiyama K. et al. (Event Horizon Telescope), 2021b, *ApJL*, 910, L13
 - [9] Medeiros L., et al., 2023, *ApJL*, 947, L7
 - [10] Akiyama K. et al. (Event Horizon Telescope), 2022a, *ApJL* 930 L12
 - [11] Akiyama K. et al. (Event Horizon Telescope), 2022b, *ApJL* 930 L13
 - [12] Akiyama K. et al. (Event Horizon Telescope), 2022c, *ApJL* 930 L14
 - [13] Akiyama K. et al. (Event Horizon Telescope), 2022d, *ApJL* 930 L15
 - [14] Akiyama K. et al. (Event Horizon Telescope), 2022e, *ApJL* 930 L16
 - [15] Akiyama K. et al. (Event Horizon Telescope), 2022f, *ApJL* 930 L17
 - [16] Kim, Jae-Young; et al., 2020. *Astronomy & Astrophysics* 640: A69
 - [17] Issaoun, S.; et al 2022 *The Astrophysical Journal*. 934 (2): 145
 - [18] Janssen M. et al. (2021). *Nature Astronomy*. 5 (10): 1017–1028
 - [19] Papoutsis E., Bauböck M., Chang D., Gammie C. F., 2023, *ApJ*, 944, 55.
 - [20] Curd B., Emami R., Anantua R., Palumbo D., Doleman S., Narayan R., 2023, *MNRAS*, 519, 2812
 - [21] Jorstad S. et al 2023 *ApJ* 943 170
 - [22] Johannsen T., 2013, *Astrophys. J.*, 777, 170
 - [23] Abdujabbarov A. A., Rezzolla L., and Ahmedov B. J., 2015, *Mon. Not. Roy. Astron. Soc.*, 454, 2423
 - [24] Abramowicz, M. A., Calvani, M. & Nobili, L., 1983, *Nature*, 302, 597–599
 - [25] Abramowicz, M.A., Jaroszyński, M. & Sikora, M. 1978, *A&A*, 63, 221
 - [26] Abramowicz, M. A., Karas, V. & Lanza, A. 1998, *A&A*, 331, 1143
 - [27] Allen, S. W., Dunn, R.J.H., Fabian, A.C., et al., 2006, *MNRAS*, 1, 372, 21
 - [28] Lu, R.S., Asada, K., Krichbaum, T.P. et al., 2023, *Nature* 616, 686–690
 - [29] Aly, H., Dehnen, W., Nixon, C. & King, A., 2015, *MNRAS*, 449, 1, 65.
 - [30] Anantua, R., et al. *Galaxies* 2023, 11, 4
 - [31] Balek V., Bica J., Stuchlik Z., 1989, *BAICz*, 40, 133
 - [32] Bardeen, J. M. 1973, in *Black Holes*, ed. C. DeWitt & B. S. DeWitt (New York: Gordon & Breach), 215
 - [33] Bardeen, J.M., Petterson, J.A., 1975, *Astrophys. J.*, 195, L65
 - [34] Bardeen J. M., Press W. H., Teukolsky S. A., 1972, *ApJ*, 178, 347.
 - [35] Beckwith K. and Done C., 2005, *Mon. Not. R. Astron. Soc.* 359, 1217
 - [36] Bica J., Stuchlik Z., Balek V., 1989, *BAICz*, 40, 65
 - [37] Broderick A. E., et al., 2022a, *ApJ*, 935, 61

calculations of the polarization configuration were generated by an orbiting toroidal source giving rise to a phenomenological model of a torus—see also [107]. In [5] it has been shown how **GRMHD** simulations produce images consistent with the **M87*** observation. [7, 8] found that only a few simulation images fit the polarimetric data (magnetically arrested disk). Semi-analytical models of the **M87** spectra were also considered in [72]. In [49] examples of semi-analytic **GRMHD** jet and accretion flow models were discussed to simulate the emission from **M87*** and **SgrA***. (The emission originates in a geometrically thick equatorial accretion flow, radiatively inefficient accretion flow and **ADAF** for **SgrA*** can fit the observed spectral energy density where different emitting regions could contribute to different regions of **M87*** and **SgrA***). Disk/jet/**BH** systems are also modelled to fit observations in particular between the co-rotating or counter-rotating (and more in general tilted) models, both with respect to the jet and for the disk components and with respect to the rotation of the central **BH**—see [8, 14, 18, 45, 49]. In [14] several astrophysical models were tested for the **SgrA*** image. In [15] the first comprehensive interpretation of the **EHT** 2017 **SgrA*** data was provided using a library of models based on time-dependent **GRMHD** simulations, in particular for aligned and tilted configurations. Physical and numerical limitations of the models were thoroughly discussed.

- [38] Broderick A. E., et al., 2022b, ApJ, 927, 6
- [39] Broderick A. E. and Loeb A., 2006, *Astrophys. J.*, 636, L109
- [40] Broderick A. E. and Narayan R., 2006, *Astrophys. J.*, 638, L21
- [41] Carter B., 1968, *Phys. Rev.*, 174, 1559
- [42] Chandrasekhar, S. *The Mathematical Theory of Black Holes*; Oxford Classic Texts in the Physical Sciences; Oxford University Press: Oxford, UK, 2002
- [43] Charbulák D., Stuchlík Z., 2018, *EPJC*, 78, 879
- [44] Chatterjee, K., Liska, M., Tchekhovskoy, A. & Markoff, S. B. 2019, *MNRAS* 490, 2200–2218
- [45] Chatterjee, K. ; Younsi, Z.; Liska et al. 2020, *MNRAS*, 499, 362–378
- [46] Crinquand B., Cerutti B., Dubus G., Parfrey K., and Philippov A., *Phys. Rev. Lett.*, 2022, 129, 205101
- [47] Doğan, S., Nixon, C., King, A. *et al.* 2015, *MNRAS*, 449, 1251
- [48] Dokuchaev V. I., and Nazarova N. O., 2020, *Physics-Uspekhi*, 63(6), 583
- [49] Emami R. et al. 2021, *Astrophys. J.* , 923, 272
- [50] H. Falcke, F. Melia, and E. Agol, *Astrophys. J.* 528, L13 (2000)
- [51] Font, J. A. & Daigne, F. 2002, *MNRAS*, 334, 383
- [52] Fragile, P. C., Blaes, et al., 2007, *Astrophys. J.*, 668, 417–429
- [53] Ghasemi-Nodehi M., Li Z.-L., and Bambi C., *Eur. Phys. J. C*, 2015, 75, 315
- [54] Gralla, S. E., Holz, D. E., & Wald, R. M. 2019, *Phys. Rev. D*, 100, 024018
- [55] Gralla, S. E., & Lupsasca, A. 2020, *Phys. Rev. D*, 101, 044031
- [56] Hamersky, J. & Karas, V., 2013, *A&A*, 32, 555
- [57] Hioki K. and Maeda, K., 2009, *Phys. Rev. D*, 80, 024042 .
- [58] Huang L., Cai M., Shen Z. Q., and Yuan F. , *Mon. Not. R. Astron. Soc.*, 2007, 379, 833
- [59] Impellizzeri C. M. V., et al., 2019, *ApJL*, 884, L28
- [60] Johnson, M. D. et al. *Science Advances*, 2020, 6, 12
- [61] Kawakatu, N., Ohsuga, K., 2011, *MNRAS*, 417, 4, 2562–2570
- [62] Kozłowski, M., Jaroszynski M. & Abramowicz, M. A. 1978, *A&A* 63, 1–2, 209–220
- [63] King A. R., Lubow S. H., Ogilvie G. I., & Pringle J. E., 2005, *MNRAS*, 363, 49
- [64] King A. and Nixon C., 2018, *Astrophys. J.* **857**, 1, L7.
- [65] King A. R., Pringle J. E. & Hofmann J. A.. 2008, *MNRAS*, 385, 1621,
- [66] Korobkin, O., Abdikamalov, E., Stergioulas, N., *et al.*, 2013, *MNRAS*, 431, 1, 354
- [67] Lasota, J.-P., Vieira, R.S.S., Sadowski, A., Narayan, R. & Abramowicz M. A. 2016, *A&A* 587, A13
- [68] Li, L. X.. 2012, *MNRAS*, 424, 1461
- [69] Liska, M., Hesp, H., Tchekhovskoy, A., *et al.* 2018, *MNRAS: Letters*, 474
- [70] Lockhart W., Gralla S. E., 2022, *MNRAS*, 517, 2462.
- [71] Lodato G. & Pringle J. E. 2006, *MNRAS*, 368, 1196
- [72] Lucchini M., Kraub F., Markoff S., 2019, *MNRAS*, 489, 1633
- [73] Luminet J. P., 1979, *Astron. Astrophys.* 75, 228
- [74] Lyutikov, M. 2009, *MNRAS*, 396, 3, 1545–1552
- [75] Madau, P. 1988, *Astrophys. J.*, 1, 327, 116–127
- [76] Martin, R. G., Pringle, J. E., & Tout, C. A. 2009, *MNRAS*, 400, 383
- [77] Misner C. W., Thorne K. S., Wheeler J. A. , 1973, *W. H. Freeman Princeton University Press*
- [78] Nealon R., Price D. and Nixon C., 2015, *Mon. Not. Roy. Astron. Soc.* **448**, 2, 1526
- [79] Nelson, R. P. & Papaloizou, J. C. B., 2000, *MNRAS*, 315, 570
- [80] Narayan, R., Johnson, M. D., & Gammie, C. F. 2019, *ApJ*, 885, L33
- [81] Nixon C., 2012, *MNRAS*, 423, 3, 2597–2600
- [82] Nixon, N. King, A. Price, D. & Frank, J. 2012, *Astrophys. J.*, 757, L24
- [83] Nixon, C., King, A. & Price, D.. 2013, *MNRAS*, 434, 1946
- [84] Oka, T., Tsujimoto, S., Iwata, Y., et al., 2017, *Nature Astronomy-Letter*,
- [85] Palumbo D.C. M. and Wong G. N. 2022 *ApJ* 929 49
- [86] Perlick V. 2004, *Living Rev. Relativ.* 7, 9
- [87] Porth, O., Chatterjee, K., Narayan, R., et al. 2019, *ApJS*, 243, 26
- [88] Pugliese, D. and Quevedo, H., 2021, *Eur. Phys. J. C*, 81, 3, 258
- [89] Pugliese D. & Stuchlík Z., 2015, *Astrophys. J.*, 221, 2, 25
- [90] Pugliese D. & Stuchlík Z., 2016, *Astrophys. J.*, 223, 2, 27
- [91] Pugliese D. & Stuchlík Z., 2017, *Astrophys. J.*, 229, 2, 40
- [92] Pugliese D. & Stuchlík Z. 2018, *Class. Quant. Grav.*, 35, 10, 105005
- [93] Pugliese D. & Stuchlík Z., 2021 *PASJ*, 73 6, 1497–1539
- [94] Pugliese D. & Stuchlík Z., 2022, *MNRAS*, 512, 4, 5895–5926
- [95] Sadowski, A., Lasota, J.P., Abramowicz, M.A. & Narayan, R. 2016, *MNRAS*, 456, 3915
- [96] Schee J., Stuchlík Z., 2009, *IJMPD*, 18, 983
- [97] Schee J., Stuchlík Z., 2009, *GReGr*, 41, 1795
- [98] Scheuer, P. A. G., & Feiler, R. 1996, *MNRAS*, 282, 291
- [99] Sikora, M. 1981, *MNRAS*, 196, 257
- [100] Stuchlík Z., Schee J., 2010, *Class. Quantum Grav.* ,27, 215017

- [101] Stuchlík Z., et al, 2021 Universe, **7**, 11
 [102] Synge J. L. 1966, Mon. Not. R. Astron. Soc. 131, 463
 [103] Tamburini, F. et al., 2020, MNRAS: Letters. 492: L22–L27
 [104] Takahashi, R., 2004, ApJ, 611, 996
 [105] Teo E., 2021, GReGr, 53, 10
 [106] Tiede P., Broderick A. E., Palumbo D. C. M., Chael A., 2022, ApJ, 940, 182.
 [107] Vincent F. H. et al. 2019 A&A 624, A52
 [108] Vincent F. H. et al. 2021 A&A 646, A37
 [109] Volonteri, M., 2007, ApJ, 663, L5
 [110] Volonteri, M., Sikora, M., Lasota, J.-P., 2007, ApJ, 667, 704
 [111] Volonteri, M., 2010, A & AR, 18, 279
 [112] White C. J., Dexter J., Blaes O., Quataert E., 2020, ApJ, 894, 14
 [113] Wielgus M. et al 2022 ApJL 930 L19
 [114] Yang H. 2012, Physical Review D 86, 104006

Appendix A: Co-rotating and counter-rotating geodesic structure

The marginally stable co-rotating (–) and counter-rotating (+) radius is

$$r_{mso}^{\mp} \equiv Z_2 + 3 \mp \sqrt{(3 - Z_1)(Z_1 + 2Z_2 + 3)}, \quad (\text{A1})$$

where

$$Z_1 \equiv (\sqrt[3]{1-a} + \sqrt[3]{a+1}) \sqrt[3]{1-a^2} + 1, \quad Z_2 \equiv \sqrt{3a^2 + \left((\sqrt[3]{1-a} + \sqrt[3]{a+1}) \sqrt[3]{1-a^2} + 1 \right)^2}. \quad (\text{A2})$$

The marginally bounded radius is

$$r_{mbo}^{\pm} \equiv \pm a + 2\sqrt{1 \pm a} + 2. \quad (\text{A3})$$

The photons circular counter-rotating and co-rotating orbits on the equatorial plane are

$$r_{\gamma}^+ \equiv 4 \cos^2 \left(\frac{1}{6} \arccos(2a^2 - 1) \right), \quad r_{\gamma}^- \equiv 2 \left[\sin \left(\frac{1}{3} \arcsin(1 - 2a^2) \right) + 1 \right]. \quad (\text{A4})$$

There is $\ell_{mso}^{\pm} \equiv \ell^{\pm}(r_{mso}^{\pm})$, $\ell_{mbo}^{\pm} \equiv \ell^{\pm}(r_{mbo}^{\pm})$ and $\ell_{\gamma}^{\pm} \equiv \ell^{\pm}(r_{\gamma}^{\pm})$ respectively, where, considering Eq. (8), there is

$$\ell^{\mp}(r) = \frac{a^3 \mp \sqrt{r^3(a^2 + (r-2)r)^2 - a(4-3r)r}}{a^2 - (r-2)^2 r}. \quad (\text{A5})$$

The location of the tori centers, r_{center}^{\pm} , is constrained by the fluids specific angular momentum ℓ , according to the radii $r_{(mbo)}^{\pm}$ and $r_{(\gamma)}^{\pm}$, defined by the relations:

$$r_{(mbo)}^{\pm} : \ell^{\pm}(r_{(mbo)}^{\pm}) = \ell^{\pm}(r_{(mbo)}^{\pm}) \equiv \ell_{mbo}^{\pm}, \quad r_{(\gamma)}^{\pm} : \ell^{\pm}(r_{(\gamma)}^{\pm}) = \ell^{\pm}(r_{(\gamma)}^{\pm}) \equiv \ell_{\gamma}^{\pm} \quad \text{where} \\ r_{\gamma}^{\pm} < r_{mbo}^{\pm} < r_{mso}^{\pm} < r_{(mbo)}^{\pm} < r_{(\gamma)}^{\pm} \quad (\text{A6})$$

respectively. On the equatorial plane, accretion tori cusps are in $\in]r_{mbo}^{\pm}, r_{mso}^{\pm}]$, with center in $r_{center}^{\pm} \in]r_{mso}^{\pm}, r_{(mbo)}^{\pm}]$. Toroids with $\mp \ell^{\pm} \equiv [\mp \ell_{mbo}^{\pm}, \mp \ell_{\gamma}^{\pm}[$ (the cusp is located in $]r_{\gamma}^{\pm}, r_{(mbo)}^{\pm}]$), have center in $r_{center}^{\pm} \in]r_{(mbo)}^{\pm}, r_{(\gamma)}^{\pm}]$. Toroids with $\mp \ell^{\pm} \geq \mp \ell_{\gamma}^{\pm}$, have centers $r_{center}^{\pm} > r_{(\gamma)}^{\pm}$ [89, 91].

Appendix B: On solutions of (\mathfrak{R})

Here we consider again solutions of (\mathfrak{R}) for $\ell \in \{\ell_{mso}^{\pm}, \ell_{mbo}^{\pm}, \ell_{\gamma}^{\pm}\}$. In order to clarify aspects of the shadow boundaries in dependence on the parameter ℓ , spin a and coordinates (r, σ) it is convenient to introduce the following quantities:

$$a_{mso}^- \equiv 0.839825, \quad a_{\lambda}^- \equiv 0.93259, \quad a_{\sigma} \equiv 0.98217, \quad \sigma_{\sigma} \equiv 0.563773, \quad \sigma_0 \equiv 0.148148, \quad (\text{B1})$$

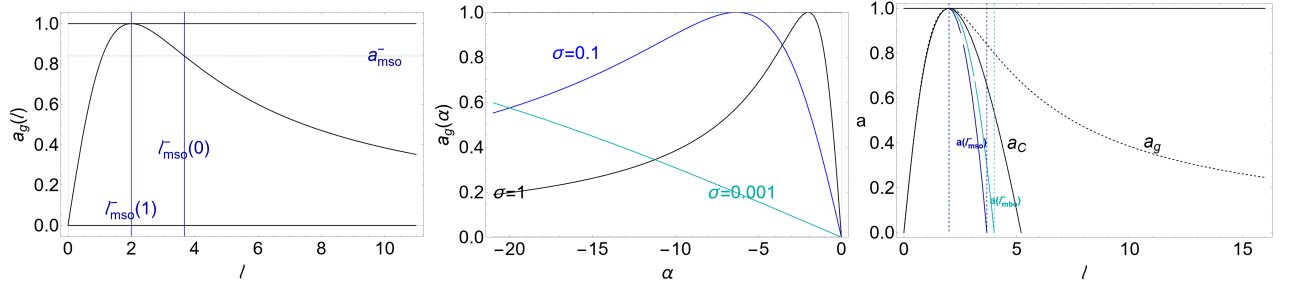


FIG. 24. Spin $a_g(\ell)$ of Eq. (B2) expression of the **BH** horizons as function of the **BH** horizons angular momentum. Spin function a_C is in Eq. (B2).

(see Figs (4)) and spin function a_C :

$$a_C \equiv \frac{3 \left(\lambda_C^{2/3} - 1 \right)}{\sqrt[3]{\lambda_C}} - \ell, \quad \text{where } \lambda_C \equiv \ell + \sqrt{\ell^2 + 1}, \quad (\text{B2})$$

see Figs (24). Quantities in Eqs (B1) and Eqs (B2), bound the constrained solutions of equations (23) we discuss below.

Case: $\ell = \ell_{mso}^-$

We consider $\ell \in [\ell_{mso}^-(a=1), \ell_{mso}^-(a=0)]^{20}$. There is then $r = 3$ for $a = 0$.

Whereas, for $a \in]0, a_g(\ell)[$, there is $r = r_\lambda$ and $q = q_\lambda$, with $q_\lambda \in]q_\lambda(a=1), q_\lambda(a=0)[^{21}$ —see Figs (2). There is $a_g(\ell_{mso}^-) \in [a_{mso}^-, 1]$, constraining the photons orbit depending on the central **BH** spin–mass ratio—Figs (24). Therefore, there is

$$\begin{aligned} \text{for } a = 0 : \quad & \sigma \in [\sigma_\ell, 1], \quad \text{where } \sigma_\ell(\ell_{mso}^-) \in [0.5, 1], \\ \text{for } a \in]0, 1] : \quad & \sigma \in [\sigma_\lambda, 1], \quad \text{where } \sigma_\lambda \in [\sigma_\lambda(a=0), \sigma_\sigma], \quad \text{and } \sigma_\lambda(a=0) = 0.5, \end{aligned} \quad (\text{B3})$$

where σ_σ is a maximum at $a = a_\sigma$ —see Figs (2). There is²²

$$q = q_\lambda : \quad \ell \in [\ell_{mso}^-(a=1), \ell_{mso}^-(a=0)], \quad (a \in]0, a_g[, r = r_\lambda); \quad (a \in]a_g, 1[, r = r_C), \quad \text{where } r_C \equiv \sqrt{a(\ell - a)}. \quad (\text{B5})$$

Similarly, using the constraint $T \geq 0$, for $a \in]0, 1]$ the solution can be written as

$$r = r_\lambda, \quad q = q_\lambda : \quad (a = a_C, \sigma = 1); \quad (a \in]0, a_C[, \sigma \in [\sigma_C, 1]); \quad (\text{B6})$$

where σ_C is a zero of the polynomial $\sum_{i=0}^6 x_i \sigma_C^i = 0$, with coefficients

$$\begin{aligned} x_0 &\equiv (a^2 - 1) \ell^6, \\ x_1 &\equiv \ell^4 [27 - a^2 (a^2 - 4a\ell + \ell^2 + 30)], \\ x_2 &\equiv a\ell^2 [-4(a^4 + 27)\ell + 96a^3 - 4a^2\ell^3 + (7a^2 + 33)a\ell^2], \\ x_3 &\equiv 2a^2[a^2(-32a^2 + 4a\ell^3 - 3\ell^4) - 3(a^4 + 22a^2 - 27)\ell^2], \\ x_4 &= \frac{a^2}{\ell^2} x_2, \quad x_5 = \frac{a^4}{\ell^4} x_1, \quad x_6 = \frac{a^6}{\ell^6} x_0, \end{aligned} \quad (\text{B7})$$

²⁰ Where $\ell_{mso}^-(a=1) = 2$ and $\ell_{mso}^-(a=0) \equiv 3.674$. This case is illustrated in the Figs (5) and Figs (6,2,4).

²¹ Where $q_\lambda(a=1) = 2.999$ and $q_\lambda(a=0) = 13.5$.

²² However, note that $r_C(\ell_\bullet) < r_+$ for $\ell_\bullet \in \{\ell_\gamma^-, \ell_{mbo}^-, \ell_{mso}^-\}$. In fact, considering the condition $T \geq 0$, the orbit $r = 3$ is for $a = 0$ on the angle $\sigma = \sigma_0$ ($\sigma_0 \neq 1$) with $q > 0$, i.e.

$$(\sigma \in]\sigma_0, 0.5], \ell \in [\ell_{mso}^-(a=1), \ell_s]), \quad (\sigma \in]0.5, 1], \ell \in [\ell_{mso}^-(a=1), \ell_{mso}^-(a=0)]], \quad \text{where, } \ell_s \equiv 5.19615\sqrt{\sigma}. \quad (\text{B4})$$

There is $\sigma_C(\ell_\bullet) = \sigma_\lambda(\ell_\bullet, q_\lambda(\ell_\bullet))$ where $\ell_\bullet = \{\ell_{mso}^-, \ell_{mbo}^-\}$ (note for $\ell_\bullet = \ell_\gamma^\pm$ there is $\sigma_C = \sigma_\lambda = 1$).

Case: $\ell = \ell_{mso}^+$

For $\ell = \ell_{mso}^+$ there is $r = r_\lambda$ and $q = q_\lambda$ for $a \in [0, 1]$. There is $\ell \in [\ell_{mso}^+(a = 1), \ell_{mso}^+(a = 0)]^{23}$, and $q_\lambda \in [q_\lambda(a = 0), q_\lambda(a = 1)]^{24}$, where

$$\text{for } a = 0: \quad \sigma \in [\sigma_\ell, 1]; \quad \text{and for } a \in]0, 1[: \quad \sigma \in [\sigma_\lambda, 1], \quad \text{where } \sigma_\lambda \in [\sigma_\lambda(a = 1), \sigma_\lambda(a = 0)], \quad (\text{B8})$$

with $\sigma_\lambda(a = 0) = 0.5$ and $\sigma_\lambda(a = 1) = 0.477$ –Figs (2).

Case: $\ell = \ell_{mbo}^+$

For $\ell \in [\ell_{mbo}^+(a = 0), \ell_{mbo}^+(a = 1)]^{25}$, for $a \in [0, 1]$, there is $r = r_\lambda$ and $q = q_\lambda$, where $q_\lambda \in [q_\lambda(a = 0), q_\lambda(a = 1)]^{26}$. Condition $T \geq 0$ implies that:

$$\begin{aligned} \text{for } a = 0: \quad & \sigma \in [\sigma_\ell, 1], \\ \text{for } a \in]0, 1[: \quad & \sigma \in [\sigma_\lambda, 1], \quad \text{where } \sigma_\lambda \in [\sigma_\lambda(a = 1), \sigma_\lambda(a = 0)], \end{aligned} \quad (\text{B9})$$

with $\{\sigma_\lambda(a = 0) = 0.591797, \sigma_\lambda(a = 1) = 0.554998\}$ –Figs (2).

Case: $\ell = \ell_{mbo}^-$

We consider the case $\ell = \ell_{mbo}^- \in [\ell_{mbo}^-(a = 1), \ell_{mbo}^-(a = 0)]^{27}$ for $a \in [0, 1]$. There is $q = q_\lambda$ and $r = r_\lambda$ where $q \in [q_\lambda(a = 1), q_\lambda(a = 0)]^{28}$.

Condition $T \geq 0$ implies that

$$\begin{aligned} \text{for } a = 0: \quad & \sigma \in [\sigma_\ell, 1], \\ \text{for } a \in]0, 1[: \quad & \sigma \in [\sigma_\lambda, 1], \quad \text{where } \sigma_\lambda \in [\sigma_\lambda(a = 0), \sigma_\lambda(a = 1)] \end{aligned} \quad (\text{B10})$$

with $\{\sigma_\lambda(a = 0) = 0.59256, \sigma_\lambda(a = 1) = 0.76391\}$.

There is $q_\lambda \in [q_\lambda(a = 1), q_\lambda(a = 0)]$, where $\{q_\lambda(a = 1) = 1, q_\lambda(a = 0) = 11\}$.

More in details there is

$$\begin{aligned} q = q_\lambda \quad \text{for} & & (\text{B11}) \\ \ell = \ell_{mbo}^-(a = 1): & \quad (a = 0, \sigma \in [\sigma_s, 1], r = 3); \quad (a \in]0, 1[, \sigma \in [\sigma_C, 1], r = r_\lambda); \quad \text{where } \sigma_s \equiv \frac{4}{27}, \\ \ell \in [\ell_{mbo}^-(a = 1), \ell_{mbo}^-(a = 0)]: & \quad (a = 0, \sigma \in [\sigma_f, 1], r = 3); \quad (a \in]0, a_C[, \sigma \in [\sigma_C, 1], r = r_\lambda); \\ & \quad (a = a_C, \sigma = 1, r = r_\lambda), \quad \text{where } \sigma_f \equiv \frac{\ell^2}{27}. \end{aligned}$$

Case $\ell = \ell_\gamma^\pm$

For $\ell = \ell_\gamma^\pm$ there are the photon circular orbits r_γ^\pm , where $q = 0$ and $\sigma = 1$.

²³ Where $\ell_{mso}^+(a = 1) = -4.4$ and $\ell_{mso}^+(a = 0) = -3.674$. This case is considered in Figs (6,2,4).

²⁴ Where $q_\lambda(a = 0) = 13.5$ and $q_\lambda(a = 1) = 20.679$.

²⁵ Where $\ell_{mbo}^+(a = 0) = -4$ and $\ell_{mbo}^+(a = 1) = -4.828$. This case is shown in Figs (7) and Figs (6,2,4).

²⁶ With $q_\lambda(a = 0) = 11$ and $q_\lambda(a = 1) = 18.2482$.

²⁷ Where $\ell_{mbo}^-(a = 1) = 2$ and $\ell_{mbo}^-(a = 0) = 4$. This case is considered in Figs (8) and Figs (6,2,4)

²⁸ With $q_\lambda(a = 1) = 1$ and $q_\lambda(a = 0) = 11$.